Journal of Computational Physics 449 (2022) 110773

Contents lists available at ScienceDirect

Journal of Computational Physics

www.elsevier.com/locate/jcp

Comparison and application of non-conforming mesh models for flow in fractured porous media using dual Lagrange multipliers ☆

Patrick Zulian [a,*], Philipp Schädle [b], Liudmila Karagyaur [a], Maria G.C. Nestola [a,c]

[a] Euler institute, USI Lugano, 6900 Lugano, Switzerland
[b] Institute of Geophysics, Department of Earth Sciences, ETH Zürich, 8092 Zürich, Switzerland
[c] Institute of Geochemistry and Petrology, Department of Earth Sciences, ETH Zürich, 8092 Zürich, Switzerland

ARTICLE INFO

Article history:
Available online 18 October 2021

Keywords:
Discrete fracture model
Non-matching meshes
Flow in fractured porous media
Finite element method
Non-conforming meshes
Lagrange multiplier method

ABSTRACT

Geological settings, such as reservoirs, include fractures with different material properties and geometric features. Hence, numerical simulations in applied geophysics demands for computational frameworks which efficiently allow us to integrate various fracture geometries in a porous medium matrix. This study focuses on a modeling approach for single-phase flow in fractured porous media and its application to different types of non-conforming mesh models. We propose a combination of the Lagrange multiplier method with variational transfer techniques for simulating flow through fractured porous media by employing complex non-conforming geometries as well as hybrid- and equi-dimensional models and discretizations. The variational transfer is based on the L^2-projection and enables an accurate and highly efficient parallel projection of fields between non-conforming meshes (e.g., between fracture and porous matrix domain).

We present the different techniques as a unified mathematical framework with a practical perspective. By means of numerical examples we discuss both, performance and applicability of the particular strategies. Comparisons of finite element simulation results to widely adopted 2D benchmark cases show good agreement and the dual Lagrange multiplier spaces show good performance. In an extension to 3D fracture network, we first provide complementary results to a recently developed benchmark case and afterwards we explore a complex scenario which leverages the different types of fracture meshes. Complex and highly conductive fracture networks are found more suitable in combination with embedded hybrid-dimensional fractures. However, thick and blocking fractures are better approximated by equi-dimensional embedded fractures and the equi-dimensional mortar method, respectively.

☆ P.Z. lead the drafting of the manuscript, implemented most methods and numerical tools, developed parts of the conceptual models, and lead parts of the numerical experiments. P.S. contributed drafting the manuscript, lead the development of the 3D conceptual models, their validation, and presentation of the results. L.K. produced, collected, and prepared most of the 2D benchmark results. M.G.C.N contributed drafting the manuscript, developed and implemented the adaptive refinement strategy and its integration with the variational transfer, lead the numerical experiments related to the adaptive refinement, and contributed to the 2D and 3D numerical experiments.

* Corresponding author.
E-mail address: patrick.zulian@usi.ch (P. Zulian).

https://doi.org/10.1016/j.jcp.2021.110773

1. Introduction

Fluid flow through fractured porous media is a crucial process in the context of numerous subsurface applications, e.g. groundwater management, geothermal energy utilization, CO_2 sequestration, hazardous waste storage, and enhanced oil and gas recovery [1–8]. Often, fluid flow velocities in fractures and in the porous medium matrix range over many orders of magnitudes. Therefore, single fractures and networks of fractures largely govern the characteristics of fluid transport in fracture-dominated porous media. More specifically, the detailed fracture geometry of each individual fracture has a significant influence on the fluid flow in a fracture-dominated system. Both the values of the aperture width of a fracture and those of the permeability of its infilling material, can vary over several orders of magnitudes. As a consequence, these two aspects lead to strong differences in the transmissivity and therefore the fractures ability to permit fluid transport. Thereby, the presence and permeability of an infilling material determines if a single fracture acts as a conduit or a barrier for fluid flow [9–12].

A detailed description of fluid flow through fractured porous media therefore requires comprehensive knowledge about the hydraulic properties of each individual fracture. Such properties are very difficult to obtain in the field and a detailed deterministic description of such systems is not possible [13]. Consequently, stochastic investigations are universally conducted to describe fractured media and to account for associated uncertainties [14,9]. Due to the large number of forward simulations required by stochastic studies, highly efficient and accurate numerical methods and mesh generation approaches are needed [15–19].

For the numerical modeling of the fractured systems, two method classes are widely used: continuum models and discrete fracture models. In the class of continuum models, fractures and porous-medium matrix are represented by separate continua within the same geometric mesh [20–23]. Effective flow properties are obtained by upscaling and information between the continua needs to be transferred. In the class of discrete fracture models, fractures are represented as discrete domains in a numerical mesh [24,25]. Here, two concepts are distinguished where the porous-medium matrix is either represented in discrete-fracture-matrix models (DFM) or neglected in discrete-fracture-networks models (DFN) [26,9]. In classic DFMs, fracture and porous-medium matrix domains are explicitly meshed and conforming at the domain interface, i.e. conforming geometry and discretization [27–30]. Due to the large complexity of fracture networks, mesh generation for such conforming DFMs can be very challenging and time consuming [31–33]. Such challenges occur in the matrix mesh domain as well as the fracture mesh domain.

Due to the large length-to-width ratio of many fractures it is common to use lower-dimensional elements to represent the fracture domain, e.g. [34–37]. This avoids elements with large aspect ratios in the fracture mesh and thus improves numerical performance. However, fractures with considerably large aperture width are not ideally represented by lower-dimensional elements [38]. Those fractures might be less numerous but require to generate fracture domain meshes which are equi-dimensional to the porous medium matrix domain. Further challenges are posed by the matrix mesh generation around the fractures. This is particularly difficult where fractures are close to each other or intersect with very small angles. Such configurations can lead to elements with large aspect ratios or non-physical connections, which requires fine tuning of the meshes to improve performance and stability of the solution [38]. It is important to bear in mind that this is even more challenging in 3D and makes stochastic studies with DFMs very difficult in practice. These challenges in model generation combined with the requirements and geometrical complexities of DFMs motivated a large number of method developments and improvements, and yielding this to be an active research field.

The drawbacks associated with the classic discrete-domain approaches have triggered research on, and the development of, numerical methods that allow to use individual meshes for the fracture and porous medium matrix domains. Such methods rely on the concept of non-conforming discretizations, while the meshes might be geometrically conforming or non-conforming. Methods with non-conforming discretization, but conforming geometries, require the element facets of the fracture domain to align with the neighboring element facets of the porous-medium matrix domain without coinciding, e.g. mortar methods [39–44] and discontinuous Galerking methods [45]. In contrast, fully non-conforming methods, i.e. non-conforming discretization and non-conforming geometry, require no geometrical relationship between the fracture and the porous-medium matrix domains. These methods exist for finite volume schemes, e.g. (p)EDFM [46–50] and for finite element schemes, e.g. extended finite element methods (XFEM) [51], or continuous Galerkin method where fractures are represented as Dirac functions [52]. XFEM approaches exist with primal formulations [53–55] and dual formulations [56,57]. An exposition of different coupling techniques in discrete fracture networks is provided in Fumagalli et al. [58], where the focus is on handling complex fracture networks without accounting the effects of the surrounding rock.

Recently, Köppel et al. [59] presented an alternative fully non-conforming finite element formulation for which Schädle et al. [60] demonstrated the applicability in 3D. Often, non-conforming mesh methods allow for an automated mesh generation and model setup process, which enables stochastic studies with a large number of different fracture network geometries. In particular, methods that handle fracture and matrix meshes separately (i.e. non-conforming geometries), significantly reduce the work required for preparing the simulation geometries. Berre et al. [61] provide a good overview of existing conceptual and discretization methods and discuss the differences in conforming and non-conforming methods.

The adoption of non-matching meshes for matrix and fracture require the use of coupling techniques and information transfer between the discretizations of the different domains. Lagrange multipliers are a common tool to couple systems of equations and they are widely used throughout various fields of research [62,63], and with state of the art techniques such as fictitious domain [64] and mortar [65–67] methods. In the context of DFMs, Lagrange multipliers have thus far

been applied for both, non-conforming discretizations with both matching and non-matching geometries. Frih et al. [68] and Boon et al. [69] presented approaches where the porous-matrix domain is split along the fracture planes. The resulting sub-domains are then meshed independently and glued together using the mortar method. Alternatively, discontinuous Galerkin methods are used to handle non-conforming interfaces between any pair of elements, hence providing flexibility at a finer granularity with respect to the mortar method [45]. A fully non-conforming approach using Lagrange multipliers to couple non-matching fracture and porous matrix discretizations is studied by Köppel et al. [59] and Schädle et al. [60]. Particularly in [60], the L^2-projection with different discrete Lagrange multipliers are used to transfer information between the fracture and porous-medium matrix domains in a variationally consistent way. Both, Köppel et al. [59] and Schädle et al. [60] studied flow through DFMs with fractures of codimension one.

While these hybrid-dimensional DFMs are widely applied and are very efficient with respect to meshing and numerical performance they are less suited for fractures with large aperture widths [38]. For such cases, equi-dimensional descriptions of the porous-medium matrix and the fractures provide more accurate results. However, this requires a volume-to-volume coupling between the fracture and the matrix discretizations. Consequently, the L^2-projection needs to be constructed considering volumetric polyhedral intersections. Volumetric coupling combined with variational transfer has been studied for several applications related to fluid-structure interaction [70,62]. Note that, as for the hybrid-dimensional case, local mass conservation is generally not guaranteed and jumping pressure coefficients can not be represented properly with our continuous Galerkin approach and Lagrange finite element spaces.

One underlying assumptions of the Lagrange multiplier approach is a continuity of the solution across the fractures, which prevents them to act as flow barriers. However, some fractures are populated with an infilling material with very low permeability and therefore hinder fluid flow. To model such fractures, equi-dimensional sub-domains with very low permeability values need to be employed and then coupled to the porous-medium matrix using the mortar method. Furthermore, Schädle et al. [60] found that the solution is less accurate in areas with fracture intersections and boundaries, which is more enhanced by steep pressure gradients located in these areas. Local adaptive mesh refinement would improve accuracy in these cases.

Schädle et al. [60] employed dual-Lagrange multipliers [66,71], which have shown to have a positive impact on the condition number and further allow to construct a symmetric positive-definite system of equations. Solving such systems is much more convenient than solving saddle-point problems, which are indefinite systems and are typically harder to solve. These types of systems can be solved with a wide range of methods, e.g., conjugate gradient method, and preconditioners, e.g. multigrid [72], and enable to perform large scale computations in a convenient manner. Furthermore, the dual-Lagrange multiplier space facilitates combining different coupling strategies, i.e. fully non-conforming hybrid-dimensional and equi-dimensional as well as mortar coupling, in a simple and unified way.

The first contribution of this paper is a unified framework based on the method of Lagrange multipliers, which combines embedded discretization methods with non-conforming domain decomposition approaches. On the one hand, embedded discretization methods are designed to couple overlapping meshes which are mutually non-conforming and can have non-matching geometric features. Here, the finite element discretization of the matrix is coupled with any number of fracture discretizations, which can be hybrid-dimensional and equi-dimensional. On the other hand, non-conforming domain decomposition techniques, such as mortar, allow us to split the domain into multiple sub-domains, discretize them independently, and couple them at their interfaces. This combination allows to employ each technique to scenarios where it is most suited, i.e. blocking fractures, fractures with large apertures, or fractures with large aspect ratio in networks with many fractures. By choosing the dual Lagrange multipliers space for each of the aforementioned coupling approaches, the arising systems of equations are easily combined and condensed, as mentioned earlier, into a unique symmetric positive-definite matrix. The second contribution of this paper consists of illustrating how to combine non-conforming adaptive mesh refinement methods with the variational transfer, and employ it to control the error as well as to reduce the number of degrees of freedom in the arising system of equations. The third contribution of this paper consists of studies of all the different approaches, both in isolation and combined. In particular, the accuracy and performance of the presented frameworks is demonstrated by comparison to standard benchmark cases in 2D and 3D as well as a complex 3D scenario which combines the different approaches.

In Section 2 we describe the overall methodology. We illustrate the unified formulation of the flow model (Section 2.1), its variational formulation (Section 2.2), the finite element discretization (Section 2.3), the necessary steps for coupling the different discretizations with dual Lagrange multipliers (Section 2.5), and the construction of the algebraic system of equations. In Section 2.6, we show how non-conforming mesh refinement can be integrated within the coupling framework, followed by some specific details about the implementation in Section 2.7. Numerical investigations and experiments are illustrated and discussed in Section 3. Finally, a conclusion of our findings and future developments are provided in Section 4.

2. Method

The method of Lagrange multipliers allows to discretize flow problems for porous media with two main types of non-conformity. First, the matrix is split into sub-domains which can be discretized independently then glued together using the mortar method [71]. Not only the sub-domains can differ in terms of permeability, but their interface can represent fractures. This case is what we refer throughout the paper as “decomposition”. Second, the fractures are represented as

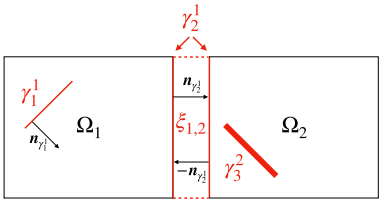

Fig. 1. Two-dimensional ($d = 2$) overview of the main geometric primitives used in this paper. Sub-domain and fracture numbers are marked with the subscript. With $\gamma_1^{d-1} = \gamma_1^1$ we denote the first fracture which is embedded and lower-dimensional. Here, γ_2^1 is a lower dimensional (line) fracture at the interface $\xi_{1,2}$, between sub-domains Ω_1 and Ω_2 of the matrix. Fractures with larger apertures are represented as equi-dimensional (polygonal) domains. With $\gamma_3^d = \gamma_3^2$ we denote an equi-dimensional fracture. With $\boldsymbol{n}_\gamma$ we denote the normal vector perpendicular to the fracture surface. The dashed lines represent a nonexistent spacing which is employed only for illustrative purposes.

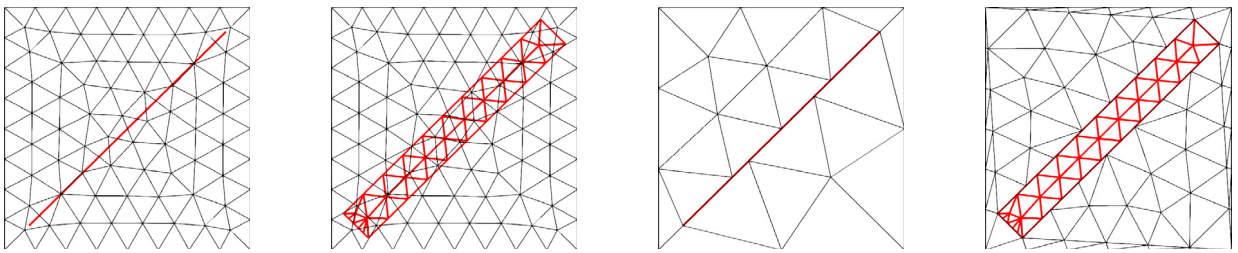

(a) Embedded-HD (b) Embedded-ED (c) Decomposition-HD (d) Decomposition-ED

Fig. 2. Different mesh representations of matrix (black) and fracture (thick/red). Left: embedded hybrid-dimensional (a) and equi-dimensional (b) fractures. Right: hybrid-dimensional (c) and equi-dimensional (d) fractures represented with domain decomposition. (For interpretation of the colors in the figure(s), the reader is referred to the web version of this article.)

separate bodies embedded in the matrix. Such fractures are described by either lower-dimensional manifolds or equi-dimensional manifolds. This case is what we refer throughout the paper as "embedded". In this section, we present a unified notation for describing the different geometric representations. Fig. 1, provides an overview of the different continuous geometric representations of both the matrix domain and fractures, the related symbols and their use are introduced in detail in Section 2.1. Fig. 2 provide simple examples for showing how the same fracture would be meshed for the different techniques.

2.1. Problem formulation

Let $\Omega \subset \mathbb{R}^d, d \in \{2, 3\}$ be the matrix domain with the following decomposition into N sub-domains

$$\overline{\Omega} = \bigcup_{i=1}^{N} \overline{\Omega}_i,$$

where $\Omega_i \cap \Omega_j = \emptyset, i \neq j$. If Ω_i and Ω_j are connected, hence $\overline{\Omega}_i \cap \overline{\Omega}_j \neq \emptyset$, their interface is described by $\xi_{ij} = \partial\Omega_i \cap \partial\Omega_j \cap \Omega$.

Let $\gamma \subset \Omega$ be a manifold of dimension d or $d-1$ describing the fracture domains with the following decomposition

$$\overline{\gamma} = \bigcup_{k=1}^{N_\gamma} \overline{\gamma}_k.$$

When required we distinguish the dimension of the manifold γ_k, with γ_k^{d-1} we have a lower-dimensional fracture, and with γ_k^d an equi-dimensional fracture. If the interface $\xi = \xi_{ij}$ is interpreted as a lower-dimensional fracture we employ the short-hand notation $\gamma_\xi = \gamma_\xi^{d-1}$.

Steady state fluid flow in the matrix Ω is governed by

$$\nabla \cdot (-\boldsymbol{K} \nabla p) - \lambda = f \qquad \text{in} \quad \Omega, \tag{1}$$

with $p = \overline{p}$ on $\partial\Omega_D$, where p is the pressure, $\boldsymbol{K} \in \mathbb{R}^{d \times d}$ is a bounded symmetric positive definite permeability tensor, f is a sink/source term, $\overline{p}$ is a given pressure on the boundary $\partial\Omega$ of the domain of interest Ω.

Flow in the fracture-network γ is described by

$$\nabla \cdot (-\boldsymbol{K}_\gamma \nabla p_\gamma) + \lambda = f_\gamma \qquad \text{in} \quad \gamma, \tag{2}$$

with $p_\gamma = \overline{p}_\gamma$ on $\partial\gamma_D$. The fluid exchange between Ω and γ is given by the Lagrange multiplier $\lambda \in \Lambda(\gamma)$. The function spaces V_Ω and V_γ are defined by

$$\begin{aligned} V_\Omega &= H^1(\Omega), \quad W_\Omega = H^1_0(\Omega), \\ V_\gamma &= H^1(\gamma), \quad W_\gamma = H^1_0(\gamma), \\ V &= V_\Omega \times V_\gamma, \quad W = W_\Omega \times W_\gamma, \end{aligned}$$

where H^1 is the Sobolev space of weakly differentiable functions, and $H^1_0 \subset H^1$ its restriction to functions vanishing at the boundary. The Lagrange multiplier space is defined as the dual of W with the product

$$\Lambda = \prod_{k=1}^{N_{\gamma^{d-1}}} H_{00}^{-\frac{1}{2}}(\gamma_k^{d-1}) \times \prod_{k=1}^{N_{\gamma^d}} H_{00}^{-1}(\gamma_k^d), \qquad N_\gamma = N_{\gamma^{d-1}} + N_{\gamma^d}.$$

With $H_{00}^{-\frac{1}{2}}(\gamma_k^{d-1})$ and $H_{00}^{-1}(\gamma_k^d)$ we describe the dual spaces of $H^{\frac{1}{2}}(\gamma_k^{d-1})$ and $H^1(\gamma_k^d)$, respectively, with zero-extension outside γ [73]. For each $\gamma_k \in \gamma$ the corresponding Lagrange multiplier is denoted with $\lambda_k \in \Lambda_k = \Lambda(\gamma_k)$.

Depending on the type of fracture the pressure term and the Lagrange multiplier have slightly different meanings. The lower-dimensional fracture, i.e., γ_k^{d-1} is associated with a thickness parameter ϵ which we consider to as a uniform scaling factor in the permeability tensor $\boldsymbol{K}_{\gamma_k} = \epsilon\kappa \boldsymbol{I}$, where $\boldsymbol{I} \in \mathbb{R}^{d\times d}$ is the identity matrix and κ is the permeability parameter. Note, that the pressure term p_{γ_k} is constant in normal direction, which is the norm for plate finite elements. We prescribe its associated Lagrange multiplier with

$$\lambda_k = [\boldsymbol{K}\nabla p \cdot \boldsymbol{n}_{\gamma_k}]_{\gamma_k} = \quad p = p(\boldsymbol{x}), \boldsymbol{x} \in \gamma_k^{d-1},$$

which represents the jump $[\cdot]$ of the fluid pressure gradient in normal direction $\boldsymbol{n}_{\gamma_k}$ with respect to the fracture surface γ_k.

For the embedded equi-dimensional fracture the Lagrange multiplier can be thought as a reactive force field introduced in order to ensure the continuity of the pressure.

At the interface $\xi = \xi_{ij}$ between the two sub-domains Ω_i and Ω_j the continuity of the solution is ensured by the following condition

$$\lambda_\xi \left(p_{\partial\Omega_i} - p_{\partial\Omega_j}\right) = 0 \qquad \text{in} \quad \xi, \tag{3}$$

where λ_ξ is the Lagrange multiplier defined on the surface ξ, and $p_{\partial\Omega_i}$ and $p_{\partial\Omega_j}$ are the pressures defined on the surfaces $\partial\Omega_i$ and $\partial\Omega_j$, respectively. The Lagrange multiplier λ_ξ is incorporated in (1) within λ as a subtracting term. With these primitives we are able to couple the different sub-domains that are discretized independently. Hence allowing also to represent fractures as sub-domains with much greater mesh resolution than the surrounding matrix. If ξ is also a fracture the additional equations

$$\nabla \cdot (-\boldsymbol{K}_{\gamma_\xi} \nabla p_{\partial\Omega_k}) + \lambda_\xi = f_{\gamma_\xi},$$

with $k \in \{i, j\}$, are added to the overall system.

Intersections between fractures are not treated explicitly hence no additional equations are added to the system.

For a more compact notation, interface fractures are not referred to explicitly since the notation is compatible and they are considered as any other fracture. Additionally, the aperture of lower dimensional fractures is neglected and considered in the permeability tensor unless stated explicitly.

2.2. Weak formulation

With $(\cdot,\cdot)_\Omega$ and $(\cdot,\cdot)_\gamma$ we denote the L^2-inner product over Ω and γ, respectively. The variational formulation is found by multiplying (1) and (2) by test functions and integrating over the domains Ω and γ, using integration by parts. Hence, the weak form of the coupled system of equations is given as follows: find $(p, p_\gamma) \in V$ and $\lambda \in \Lambda$, such that

$$(\boldsymbol{K}\nabla p, \nabla q)_\Omega + (\boldsymbol{K}_\gamma \nabla p_\gamma, \nabla q_\gamma)_\gamma - (\lambda, q - q_\gamma)_\gamma = (f, q)_\Omega + (f_\gamma, q_\gamma)_\gamma \quad \forall (q, q_\gamma) \in W, \tag{4}$$

and the weak equality condition

$$(p - p_\gamma, \mu)_\gamma \qquad \forall \mu \in \Lambda, \tag{5}$$

are satisfied.

2.3. Discretization

The variational formulation introduced in Section 2.2 is discretized using the finite element method. Depending on the settings different meshes $\mathcal{M}_i = \mathcal{M}_{\Omega_i}$ and $\mathcal{M}_{\gamma_k}$ are used for the different sub-domains of the porous matrix $\Omega_i, i = 1, \dots N$, and for the fractures $\gamma_k, k = 1 \dots N_\gamma$ respectively. The presented techniques and their implementation allow for an arbitrary choice of $\mathcal{M}_{\lambda_k}$, which is the mesh associated with the Lagrange multiplier, however since we restrict ourselves to a particular choice of multiplier space, we set $\mathcal{M}_{\lambda_k} = \mathcal{M}_{\gamma_k}$.

The method allows for a wide variety of elements for each of the meshes. For a manifold with dimension d we employ either Lagrange elements $\mathbb{P}^k$, or tensor-product elements $\mathbb{Q}^k$ of order $k \in \{1, 2\}$

$$\begin{aligned} W_{h,\alpha} = \{ & w \in W(\alpha) : \forall E \in \mathcal{M}_\alpha, \\ & w|_E \in \begin{cases} \mathbb{P}^k & \text{if } E \text{ is a simplex} \\ \mathbb{Q}^k & \text{if } E \text{ is a hyper-cuboid} \end{cases} \\ & \}, \\ & \alpha \in \{\Omega, \gamma^d, \gamma^{d-1}\} \\ \Lambda_{h,\beta} \quad & \beta \in \{\gamma^d, \gamma^{d-1}\}, \end{aligned} \tag{6}$$

where Λ_h is a discrete Lagrange multiplier space. Let $\{\varphi_i\}_{i \in J}$ be a basis of $W_{h,\Omega}$, $\{\theta_j\}_{j \in J_\gamma}$ a basis of $W_{h,\gamma}$, and $\{\psi_k\}_{k \in J_\gamma}$ a basis of Λ_h, where J and $J_\gamma \subset \mathbb{N}$ are index sets of the node-sets of their respective meshes $\mathcal{M}$ and $\mathcal{M}_\gamma$. Writing the functions $q \in W_{h,\Omega}$, $q_\gamma \in W_{h,\gamma}$, and $\mu \in \Lambda_{h,\gamma}$ in terms of their respective bases and coefficients, they read $q = \sum_{i \in J} q_i \varphi_i$, $q_\gamma = \sum_{j \in J_\gamma} q_{j\gamma} \theta_j$, and $\mu = \sum_{k \in J_\gamma} \mu_{k\gamma} \psi_k$.

The dual shape functions $\psi_j \in \Lambda_h(\gamma)$ are constructed in such a way that they satisfy the bi-orthogonality condition [71]:

$$(\theta_i, \psi_j)_{\gamma_h} = \delta_{ij} (\theta_i, 1)_{\gamma_h} \qquad \forall i, j \in J_\gamma, \tag{7}$$

where δ_{ij} is the Kronecker delta function, and integral positivity

$$(\psi_j, 1)_{\gamma_h} > 0. \tag{8}$$

Note that (8) is naturally satisfied for first order finite elements. For second order elements we follow the construction described in [66,74].

After reformulating the variational problem (4) as a set of point-wise algebraic equations, the discrete problem for the porous matrix reads:

$$\sum_{i \in J} p_i (\mathbf{K} \nabla \varphi_i, \nabla \varphi_j)_{\Omega_h} - \sum_{k \in J_\gamma} \lambda_k (\psi_k, \varphi_j)_{\gamma_h} = (f, \varphi_j)_{\Omega_h}, \qquad \forall j \in J, \tag{9}$$

which translates to the linear system $\mathbf{A}\mathbf{p} - \mathbf{B}^T \boldsymbol{\lambda} = \mathbf{f}$. The fracture equations result in,

$$\sum_{i \in J} p_{i,\gamma} (\mathbf{K}_\gamma \nabla \theta_i, \nabla \theta_j)_{\gamma_h} + \sum_{k \in J_\gamma} \lambda_k (\psi_k, \theta_j)_{\gamma_h} = (f_\gamma, \theta_j)_{\gamma_h}, \qquad \forall j \in J_\gamma, \tag{10}$$

which translates to the linear system $\mathbf{A}_\gamma \mathbf{p}_\gamma + \mathbf{D}^T \boldsymbol{\lambda} = \mathbf{f}_\gamma$. The weak-equality condition (5) results in,

$$-\left(\sum_{i \in J} p_i (\varphi_i, \psi_j)_{\Omega_h} - \sum_{k \in J} p_{k,\gamma} (\theta_k, \psi_j)_{\gamma_h} \right) = 0, \qquad \forall j \in J_\lambda, \tag{11}$$

which translates to the linear system $-\mathbf{B}\mathbf{p} + \mathbf{D}\mathbf{p}_\gamma = \mathbf{0}$. The discretization of the complete problem results in saddle-point system as follows:

$$\begin{vmatrix} \mathbf{A} & \mathbf{0} & -\mathbf{B}^T \\ \mathbf{0} & \mathbf{A}_\gamma & \mathbf{D}^T \\ -\mathbf{B} & \mathbf{D} & \mathbf{0} \end{vmatrix} \begin{vmatrix} \mathbf{p} \\ \mathbf{p}_\gamma \\ \boldsymbol{\lambda} \end{vmatrix} = \begin{vmatrix} \mathbf{f} \\ \mathbf{f}_\gamma \\ \mathbf{0} \end{vmatrix}. \tag{12}$$

Due to the choice of Lagrange multipliers, following the definition in (11), the matrix $\mathbf{D}$ is trivially invertible. For linear elements $\mathbf{D}$ is in fact diagonal and for quadratic element the inverse is constructed as a combination of a basis transformation, for which its inverse is known [66], and again a diagonal matrix. This convenient property enables us to perform block Gaussian elimination and obtain the following statically condensed system [75]

$$(\mathbf{A} + \mathbf{T}^T \mathbf{A}_\gamma \mathbf{T}) \mathbf{p} = \mathbf{f} + \mathbf{T}^T \mathbf{f}_\gamma, \tag{13}$$

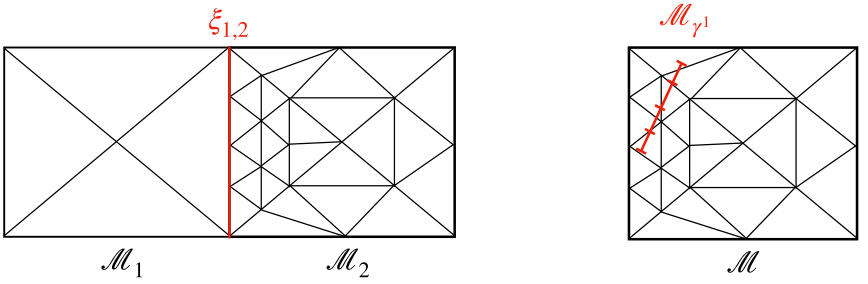

(a) Non conforming interface $\xi_{1,2}$ between mesh $\mathcal{M}_1$ and mesh $\mathcal{M}_2$.

(b) Meshes for fracture $\mathcal{M}_{\gamma^1}$ and porous matrix $\mathcal{M}$ for the embedded scenario.

Fig. 3. Non-conformity with matching geometry (a) and non-matching geometry (b).

Table 1
Intersection for different coupling types. The standard mortar and nonmortar roles used in the related literature are associated with matrix and fracture, respectively.

Matrix (mortar)	Fracture (nonmortar)	Intersection type
$\Omega \subset \mathbb{R}^3$	γ^3	polyhedron-polyhedron
$\Omega \subset \mathbb{R}^3$	γ^2	polyhedron-polygon
$\partial\Omega_i \cap \xi_{i,j} \subset \mathbb{R}^3$	$\partial\Omega_j \cap \xi_{i,j} \subset \mathbb{R}^3$	polygon-polygon (oriented)
$\Omega \subset \mathbb{R}^2$	γ^2	polygon-polygon
$\Omega \subset \mathbb{R}^2$	γ^1	polygon-segment
$\partial\Omega_i \cap \xi_{i,j} \subset \mathbb{R}^2$	$\partial\Omega_j \cap \xi_{i,j} \subset \mathbb{R}^2$	segment-segment (oriented)

where $\mathbf{T} = \mathbf{D}^{-1}\mathbf{B}$. Once the system is solved for $\mathbf{p}$, the solution for the fracture network can be computed by $\mathbf{p}_\gamma = \mathbf{T}\mathbf{p}$. The resulting system matrix is symmetric positive definite which allows us to adopt optimal solution strategies such as Multigrid methods [72].

2.4. Handling multiple types of non-conforming mesh interactions

The presented methods handle non-conforming meshes in two stages. The first stage involves the domain decomposition of the porous matrix. For instance, a matrix domain Ω can be split into the two domains Ω_1 and Ω_2 with interface $\xi_{1,2}$, this interface could be interpreted as a fracture. However, in discrete settings (Fig. 3 (a)) it could also be a convenient way to handle different resolutions for the meshes $\mathcal{M}_1$ and $\mathcal{M}_2$, and ensure the continuity of the solution at $\xi_{1,2}$ using the standard mortar approach introduced in Bernardi et al. [65]. In practice, we need to assign the standard mortar and nonmortar role, for instance, we assign the mortar role to ξ_1 and nonmortar role to ξ_2. Once the transfer operator is assembled the porous-medium-matrix system is condensed. Note that in the resulting system of equations the degrees of freedom associated with the nonmortar discretization are eliminated after static condensation (e.g., by replacing the related rows of the matrix with the identity and the related right-hand side value with zero). Once this is achieved we go to the next stage.

The second stage involves the embedded case (Fig. 3(b)) where we compute the transfer operator between W_h and $W_{h,\gamma}$ and condense the resulting system as described in Section 2.3.

2.5. Information transfer

The computation of the so called mortar integrals, which are the integral terms in (9), (10), and (11), associated with the Lagrange multiplier require special handling. In fact, quadrature formulas have to be generated in the intersection between elements of the matrix and the fracture. The computation of intersections differs depending on which type of fracture is considered. Table 1 lists, for each type of coupling, the roles and the intersection types. Here, the mortar role is given to the domain covering completely the nonmortar domain. The nonmortar role is given to the domain with which we associate the Lagrange multiplier space.

For the coupling at an interface ξ, either for non-conforming domain decomposition or for an interface fracture γ_ξ, the coupling is performed on a common surface description. This operation requires intersecting oriented planar polygonal elements in the case of a three-dimensional problem, or intersecting oriented line elements in the case of two-dimensional problem.

For the embedded scenario, the polytopal elements of the matrix are intersected with the lower- or equi-dimensional polytopal elements of the fracture. The case where we have $\mathcal{M} \subset \mathbb{R}^d$ and $\mathcal{M}_\gamma$ being a $(d-1)$-dimensional manifold mesh, requires particular handling when the fracture elements are aligned with the surface of the matrix elements. In such case it is likely that some intersections might be computed twice, hence these duplicate intersections are detected and removed.

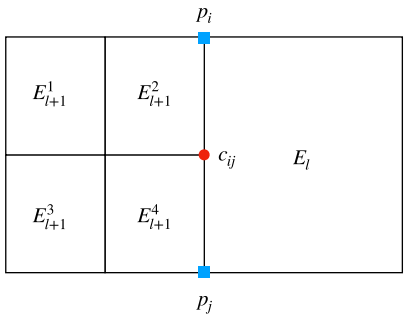

Fig. 4. Bi-linear elements E^k with different levels of refinement $k \in \{l, l+1\}$. With p_i, p_j we denote the parent nodes that are generated on level l, with $c_{ij} = (p_i + p_j)/2$ we denote the child node generated on level $l+1$ by splitting the edge (i, j). Depending on the finite element discretization the splitting is done in different (multiple) locations. The prolongation operation at node c_{ij} for this particular case would simply be $u(c_{ij}) = (u(p_i) + u(p_j))/2$.

The $(d-1)$-dimensional fractures represented with the mortar method require a careful set-up. In fact, in the case of intersecting fractures, multiple sub-domains (more than two) might intersect at one point or edge. The mesh primitives, i.e. edges and nodes, generating such intersections require a specific handling. The first approach consists of ignoring the side elements that are incident to the aforementioned mesh primitives when defining the discrete Lagrange multiplier as in Krause et al. [76], hence introducing discontinuities of the solution at these interfaces. The second approach, which would require a set-up similar to Farah et al. [77], consists of defining one-to-many relationships for the intersecting primitives. Here, one mortar primitive has to be determined and continuity is either enforced using interpolation for intersecting nodes, or with a weak equality condition for intersecting edges. The third approach, consists of explicitly defining the entire surface mesh for which the discrete Lagrange multiplier is constructed. These complications with the mortar method are not present in the equi-dimensional case if the discrete fractures are represented with a unique conforming mesh, since the role of mortar and nonmortar can be trivially assigned to porous-matrix and fracture respectively.

The computation of the intersections listed in Table 1 is performed with suitable variants of the Sutherland-Hodgman clipping algorithm [78]. Once the intersection is computed, if required, this intersection is meshed into a simplicial complex so that we can map quadrature rules to each simplex and integrate exactly.

2.6. Adaptive refinement

Let us recall the definition of element E from Section 2.3. With ∂E we denote the boundary of element E and with $\bar{E}$ its closure. A mesh is said to be conforming if $\bar{E}_i \cap \bar{E}_j, i \neq j$ is a common vertex, edge, face, or $\emptyset$. A node is said to be hanging if it lies on the interior of an edge or face of another element. A mesh containing at least one hanging node is called non-conforming.

Non-conforming adaptive mesh refinement has the advantage that can be applied to any type of element in a rather straight-forward and independent manner. However, once the elements marked by the error estimator are refined, the resulting mesh might have hanging nodes, as shown in Fig. 4.

As a consequence, continuity of the solution is to be enforced either by employing variational restriction or adopt discontinuous Galerkin methods. Here, we consider the variational restriction technique which is thoroughly explained in Cerveny et al. [79] also for high-order discretizations.

Let $\mathbf{R}_i, i \in \{m, s\}$ be a suitable restriction operator that splits contributions of each hanging node to its adjacent nodes, where m stands for matrix and s refers to the fracture. For combining adaptivity with DFMs and the method of Lagrange multipliers, we consider the constrained spaces arising from the refinement and variational restriction, which requires us to perform some slight modifications to the final steps of the assembly procedure for the transfer operator, in any of the cases we mentioned in previous sections. We recall the definitions of the coupling matrix $\mathbf{B}$ and mass-matrix $\mathbf{D}$ from Section 2.3, and define the modified transfer operator

$$\mathbf{T}_R = (\mathbf{R}_s^T \mathbf{D} \mathbf{R}_s)^{-1} (\mathbf{R}_s^T \mathbf{B} \mathbf{R}_m).$$

The operator $\mathbf{T}_R$ allows us to transfer between constrained spaces, however for also setting the values in the hanging nodes we apply the prolongation operator $\mathbf{P}_s = \mathbf{R}_s^T$ as follows

$$\mathbf{T} = \mathbf{P}_s \mathbf{T}_R.$$

This small modification allows to use $\mathbf{T}$ as in the standard case without any special treatment as described in Section 2.2.

2.7. Implementation

The routines described in this paper are implemented within the open-source software library *Utopia* [80,81]. In this work, *Utopia* uses *libMesh* [82] for the finite element discretization, *MOONoLith* [83] for the intersection detection, and

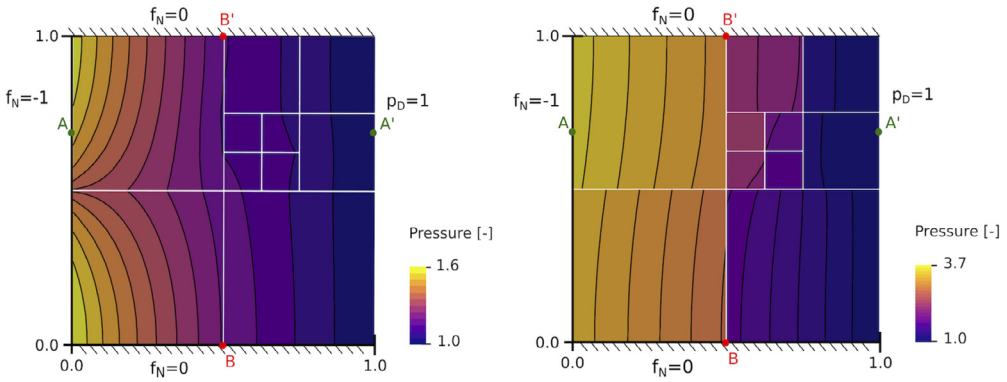

(a) Embedded/conductive (b) Decomposition/blocking

Fig. 5. *2D Benchmark Case 1: Regular fracture network*, from Flemisch et al. [38]. Pressure solution for a regular fracture network with six equi-dimensional fractures for conductive fractures with the equi-dimensional embedded method (a) and blocking fractures with the equi-dimensional decomposition method (b).

PETSc [84] for the linear algebra calculations. The software developed for this contribution is used by means of a JSON (JavaScript Object Notation) input file where any number of mesh files can be linked to the simulation and coupled together automatically for creating complex networks of fractures.

3. Numerical results & discussion

First, the focus is on a comparison of results obtained with the equi-dimensional embedded technique and the mortar method to a specific selection of commonly used 2D and 3D benchmarks [38,85]. Here, we use non-conforming mesh refinement in proximity of the fractures for maintaining the size of the mesh small while achieving small deviations from the reference solution. Second, we show how employing an adaptive mesh refinement, with gradient-recovery based error estimator [86], allows us to refine only where the error in the solution is estimated to be higher. Finally, we present a complex 3D experiment inspired by realistic scenarios where we conveniently mix all the techniques we covered in this article. In each of the following sections we discuss the practicalities of the different techniques and how to combine them.

For compactness, in the following sections we use the abbreviation ED for equi-dimensional and HD for hybrid-dimensional. We report exclusively the error of the solution associated with the matrix discretization. This is done for avoiding redundant information, since the solution for the fracture is just the L^2-projection of the solution for the matrix.

3.1. 2D benchmarks

The 2D setting allows us to provide a simpler and clearer presentation of the numerical results. Hence, with a selection of 2D benchmarks from Flemisch et al. [38], we complement and extend the previous contribution presented in Schädle et al. [60]. We verify the embedded ED approach and our implementation of the mortar method with the dual Lagrange multiplier. We show how adaptive mesh refinement allows us to solve problems with a smaller number of degrees of freedom while achieving the desired accuracy in the solution. For all 2D cases we use the reference solution p_{ref} proposed in Flemisch et al. [38] which is computed by means of the mimetic finite difference method. Consistent with the analysis proposed in [38], the numerical error is computed as

$$\mathbf{err}_m = \frac{\int_\Omega (p - p_{\text{ref}})^2}{(\max(p_{\text{ref}}) - \min(p_{\text{ref}}))^2 \int_\Omega 1}.$$

3.1.1. 2D benchmark case 1: regular fracture network

We consider the same settings and reference solutions used in Flemisch et al. [38] *Benchmark 1*, with both conductive and blocking fractures, as shown in Fig. 5. Both settings have the same square domain $\Omega = [0, 1]^2$ and boundary conditions. We impose Dirichlet conditions on the right boundary, where the pressure is set to constant value 1. We impose no-flow conditions on the bottom and top sides. Permeability of the matrix is uniform $\mathbf{K} = \mathbf{I}$, where $\mathbf{I}$ is the identity matrix. We distinguish conductive and blocking scenarios for the fracture permeability. For the conductive scenario, in the HD case the permeability tensor is described as $\mathbf{K}_{\gamma^1} = \epsilon \mathbf{I} \cdot 10^4$, where $\epsilon = 10^{-4}$ is the fracture aperture, whereas for the ED case we have $\mathbf{K}_{\gamma^2} = \mathbf{I} \cdot 10^4$. For the blocking scenario, we only have the ED case with $\mathbf{K}_{\gamma^2} = \mathbf{I} \cdot 10^{-4}$.

A particular emphasis is placed on equi-dimensional fractures and the comparison between non-conforming embedded/immersed fractures and geometrically conforming fractures which are glued together with the matrix using the mortar method. For the hybrid-dimensional embedded we reproduced the results of Schädle et al. [60] using the methods of dual-Lagrange multipliers and static condensation. In Table 2, we report results for three different resolutions for each of the

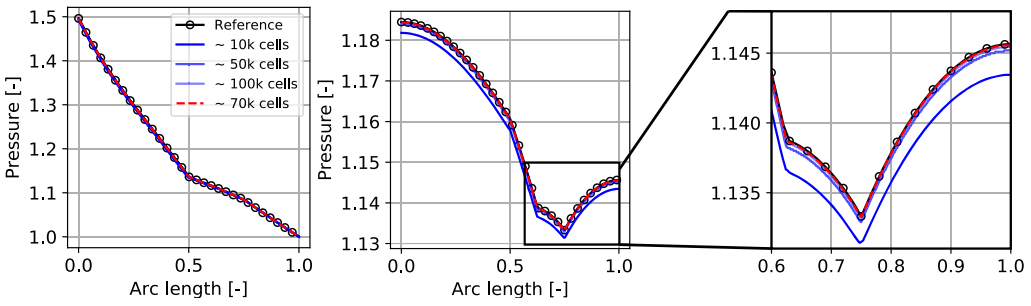

(a) Line AA′ (b) Line BB′

Fig. 6. *2D Benchmark Case 1: Regular fracture network.* Pressure profiles along the lines AA′ (a) and BB′ (b) with a zoom into the area with the largest deviation. Blue lines indicate Emebedded-ED, dashed red lines indicate Decomposition-ED.

Table 2
2D Benchmark Case 1: Regular fracture network. For each method we report number of elements in the matrix (**#-matr**) and fracture (**#-frac**), number of degrees of freedom (**d.o.f.**), normalized number of non zero entries (**nnz/size**^{2}), condition number ($\|\cdot\|_2$-**cond.**) and error in the matrix (**err**$_m$) with respect to the reference solution.

Method	#-matr.	#-frac.	d.o.f.	nnz/size^2	$\|\cdot\|_2$-cond.	err$_m$
Embedded-ED	10 656 triangles	8648	5853	2.6e-4	3.7e6	3.3e-5
Embedded-ED	47 142 triangles	8648	25 992	7.6e-5	1.8e8	1.9e-6
Embedded-ED	96 762 triangles	8648	53 379	5.3e-5	1.2e9	2.8e-7
Decomposition-ED	12 791 triangles	34 592	32 935	2.3e-4	5.2e10	6.4e-8
Decomposition-ED	36 331 triangles	34 592	45 172	1.7e-4	8.8e10	2.8e-8
Decomposition-ED (blocking)	922 triangles	34 592	26 520	2.7e-4	9.4e7	3.3e-8
Embedded-HD	1600 quads	112	1681	9.7e-4	1.6e5	1.3e-7
Embedded-HD	25 600 quads	448	25 921	4.3e-5	9.5e6	1.0e-7
Embedded-HD	102 400 quads	896	103 041	1.0e-5	7.6e7	9.8e-8
Embedded-ED (disconnected)	7596 triangles	12 052	4198	3.2e-4	2.0e6	6.1e-5
Embedded-ED (disconnected)	34 116 triangles	12 052	18 902	7.7e-5	4.1e7	4.0e-6
Embedded-ED (disconnected)	70 365 triangles	12 052	38 998	4.6e-5	2.6e8	8.9e-7
Embedded-HD (disconnected)	1600 quads	112	1681	8.5e-4	1.6e5	2.9e-7
Embedded-HD (disconnected)	25 600 quads	448	25 921	4.3e-5	9.6e6	2.3e-7
Embedded-HD (disconnected)	102 400 quads	896	103 041	1.0e-5	7.6e7	2.2e-7

three strategies. Here, we differentiate with fractures that are represented as a unique connected mesh as well as disconnected entities. In the following paragraphs we illustrate the different set-ups, results, and limitations of the embedded and mortar methodologies.

The employed embedded techniques enforce the continuity of the solution at the intersection of the matrix and fracture meshes. Hence, steep pressure jumps and barriers can not be represented. Consequently, for the embedded case we restrict our study to conductive fractures. In particular, we study the equi-dimensional embedded technique for 3, 5, and 6 levels of non-conforming mesh refinement (Section 2.6) performed exclusively in proximity of the fractures. This refinement patterns are generated automatically using the variational transfer algorithm for marking the elements of the matrix that are intersecting with the fractures. On Fig. 6, we plot the solution over the lines AA′ (y = 0.75) and BB′ (x = 0.5) and it can be observed that even for low resolutions, the solutions are in agreement with the reference results of Flemisch et al. [38]. From Table 2, it can be observed that with this particular set-up we reach an error in the order of 10^{-7} for both connected and disconnected fracture networks. Note that the number of elements in the fracture network do not influence the number of degrees of freedom, hence they do not count for the computational cost of solving the linear system but only for the set-up phase which is typically cheaper.

For the domain decomposition technique based on the classical mortar method we are required to represent the fracture explicitly in the matrix mesh. For this particular scenario, the fracture is modeled as an equi-dimensional geometry which is meshed independently from the matrix. This allows us to refine all the different sub-domains in a completely independent manner and glue them together using the mortar method. We manually refine the matrix around the two fractures crossing at the center of the domain. This is done for having a higher resolution in the region of interest of the benchmark. From Table 2, it can be observed that even for low mesh resolutions of the matrix the error reaches an order of 10^{-8} for both, conductive and blocking fractures. However, the mesh resolution of the fractures is very high from the start. Despite this

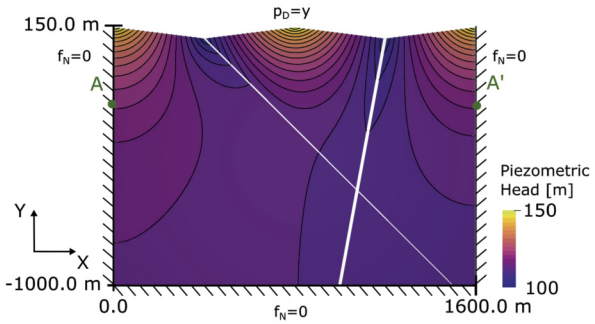

Fig. 7. *2D Benchmark Case 2: Hydrocoin*, from Flemisch et al. [38]. Embedded-ED: spatial distribution of the piezometric head [m]. Solution profiles are compared along the line AA′ with coordinates $y = -200$ [m] (marked in green).

Table 3
2D Benchmark Case 2: Hydrocoin. Uniform refinement for the Embedded-ED vs Decomposition-ED cases. Here $\mathbf{err}_m$ is the error computed with respect to the reference solution. **#UR** refers to the number of uniform refinements.

Method	#-matr.	#-frac.	d.o.f.	nnz/size^2	$\|\cdot\|_2$-cond.	err_m	#UR
Embedded-ED	272 triangles	3 480	159	4.3e-2	2.83e3	4.6e-4	1
Embedded-ED	1 088 triangles	3 480	589	1.2e-2	2.12e4	7.3e-5	2
Embedded-ED	4 352 triangles	3 480	2 265	3.1e-2	1.35e5	1.3e-5	3
Embedded-ED	17 408 triangles	3 480	8 881	8.1e-4	9.13e5	2.25e-6	4
Embedded-ED	69 632 triangles	3 480	35 169	2.1e-4	5.02e6	6.73e-7	5
Embedded-ED	278 528 triangles	3 480	139 969	5.5e-5	2.07e7	2.28e-7	6
Decomposition-ED	1 116 triangles	220	246	9.7e-3	3.6e6	4.5e-5	1
Decomposition-ED	4 464 triangles	880	2 973	2.5e-3	7.6e6	7.5e-6	2
Decomposition-ED	17 856 triangles	3520	11 285	6.4e-4	2.7e7	1.1e-6	3
Decomposition-ED	71 424 triangles	14 080	43 941	1.7e-4	1.1e8	1.5e-7	4

fact, in our experiments the actual degrees of freedom are only associated with one layer of nodes in the middle of the fracture, while the ones at the interface are eliminated by means of the mortar constraints as mention in Section 2.4.

We can observe that the embedded methodologies generate linear systems with comparable condition numbers and number of degrees of freedom. Whereas, the decomposition-ED method gives rise to larger systems with larger condition numbers. Only with the decomposition-ED we are able to solve the blocking scenario 5(b), however already for this simple experiment the mesh set-up is more laborious due to the matching geometry.

3.1.2. 2D benchmark case 2: hydrocoin

We test the capability of the adaptive mesh refinement by considering the hydrocoin benchmark [87] for two different techniques: the embedded-ED and the decomposition-ED. The matrix consists of a rectangular box with a broken line located on the top, whereas the fracture network consists of two oblique lines. As shown in Fig. 7, we prescribe the piezometric head on the Dirichlet boundary on the top and Neumann no-flow on the remaining sides of the rectangular box. The permeability is set equal to $\mathbf{K}_\gamma = 10^{-6}$ [m/s] for the fractures and $\mathbf{K} = 10^{-8}$ [m/s] for the matrix. Fracture aperture is about $\epsilon_1 = 10.16$ for the left fracture and about $\epsilon_2 = 15$ for the right fracture.

We use a gradient recovery strategy for the a-posteriori error estimation to guide the adaptive refinement (AR) of the matrix and the fracture meshes, and compare the numerical results with those computed employing uniform refinement (UR). We estimate the accuracy of each numerical simulation by computing the error with respect to the reference solution obtained on a very fine mesh consisting of 2 745 606 nodes.

In Tables 3, 4 and 5 we report the results related to the embedded-ED technique for UR and AR test cases, respectively. Here, all the methods provide numerical solutions converging to the reference one. In particular, we specify the number of elements in the matrix mesh (**#-matr.**) and in the fracture mesh (**#-frac.**), the number of degrees of freedoms (**d.o.f.**), the density of non zeros entries (**nnz/size**^{2}), the condition number ($\|\cdot\|_2$**-cond**), and the error computed with respect to the reference solution ($\mathbf{err}_m$). In Table 3 we also specify the number of uniform refinements (**#UR**), whereas in Tables 4 and 5 we report the number of adaptive refinements (**#AR**), and the error-threshold used for the gradient recovery strategy ($\mathbf{err}_g$). We point out that both the UR and the AR strategies are only performed on the matrix mesh.

In Table 4 we also compare the condition number of the original stiffness matrix with the one obtained by using left inverse diagonal scaling (IDS), i.e., $\tilde{m}_{ij} = m_{ij}/m_{ii}$, where m_{ij} and $\tilde{m}_{ij}$ are the entries of the system matrix and the preconditioned one, respectively. As one may observe the use of such a preconditioner allows to reduce the condition number of several magnitudes. This result suggests that the AR strategy is a viable option to reduce the computational costs without affecting the properties of the stiffness matrix of the overall systems of equations.

Table 4
2D Benchmark Case 2: Hydrocoin. Adaptive refinement for the Embedded-ED cases. Here, $\mathbf{err}_g$ is the threshold used for the gradient recovery strategy. #**AR** refers to the number of adaptive refinements, whereas the number within parentheses refers to the steps of adaptive refinement performed on the overlapping region between the matrix and the fracture meshes.

Method	#-matr.	#-frac.	d.o.f.	nnz/size^2	$\|\cdot\|_2$-cond	IDS-cond	err_m	# AR	err_g
Embedded-ED	611 triangles	3 480	352	2.0e-2	1.5e10	1.3e04	7.8e-5	0 (2)	-
Embedded-ED	1 544 triangles	3 480	874	7.8e-3	5.3e10	3.3e04	1.2e-5	1 (2)	5
Embedded-ED	2 378 triangles	3 480	1354	4.5e-3	8.1e10	5.1e04	5.8e-6	2 (2)	5
Embedded-ED	7 913 triangles	3 480	4371	1.6e-3	3.5e11	3.2e05	1.8e-6	4 (2)	1
Embedded-ED	9 147 triangles	3 480	5006	1.5e-3	2.8e11	7.4e05	1.1e-6	4 (4)	1
Embedded-ED	21 599 triangles	3 480	11658	1.02e-3	1.06e12	5.3e06	2.6e-7	4 (6)	1

Table 5
2D Benchmark Case 2: Hydrocoin. Adaptive refinement for the Decomposition-ED cases. Here, $\mathbf{err}_g$ is the threshold used for the gradient recovery strategy. #**AR** refers to the number of adaptive refinements, whereas the number within parentheses refers to the steps of adaptive refinement performed on the overlapping region between the matrix and the fracture meshes.

Method	#-matr.	#-frac.	d.o.f.	nnz/size^2	$\|\cdot\|_2$-cond.	err_m	# AR	err_g
Decomposition-ED	2 127 triangles	202	1375	5.9e-3	1.3e11	4.7e-5	1 (1)	5
Decomposition-ED	8502 triangles	727	2791	1.1e-3	2.5e11	8.6e-6	2 (1)	1
Decomposition-ED	17 826 triangles	1942	10 600	7.1e-4	7.1e11	1.1e-6	3 (0)	0.2
Decomposition-ED	71424 triangles	2500	15 284	4.8e-4	5.36e12	1.3e-7	4 (0)	0.1

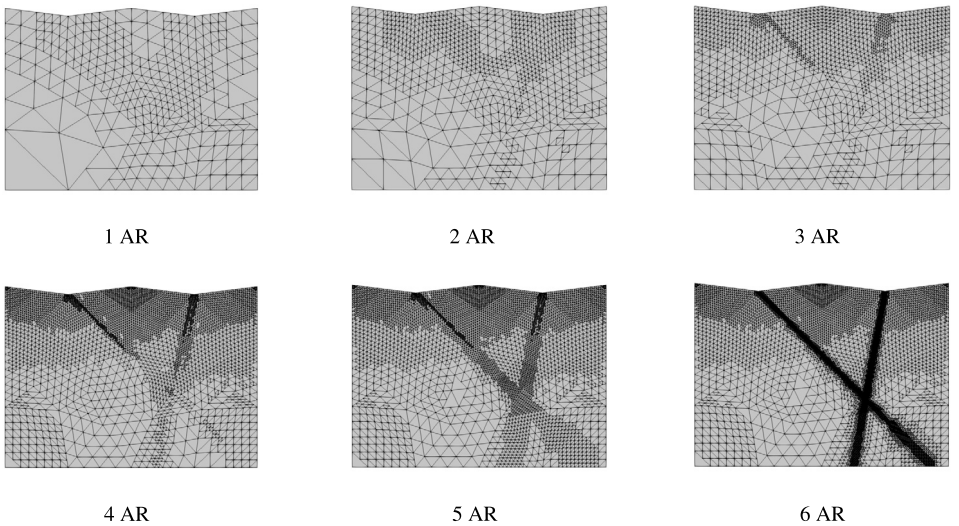

Fig. 8. *2D Benchmark Case 2: Hydrocoin.* Embedded-ED adaptive mesh refinement. The meshes have been obtained by performing first an adaptive refinement in the region where fractures are located, then by using the gradient-recovery based error estimator.

In Fig. 8 we show the meshes obtained for all the six AR test cases. The AR based on the gradient recovery strategy is combined with an AR performed on the overlapping region between the matrix and the fracture network. The number of AR performed in the overlapping zone are reported in Tables 4 and 5 and specified within parentheses.

Fig. 9 shows the piezometric head obtained over line AA′ for the UR (a) and the AR (b) test cases. One may note large discrepancies in the area of the left fracture, especially for the results referred to the uniform refined meshes. In this regard, we found that the a-posteriori error $\mathbf{err}_g$ was higher close the sharp top boundary and in the zone occupied by the left fracture. Indeed, Fig. 8 (3)-(5) show that the AR strategy produces a mesh size reduction in such regions. Hence, all the AR test cases reveal a better agreement with the reference solution when compared to the UR scenarios.

For completeness, the numerical results obtained for the test case 3 AR are presented in Fig. 7. Here, the color refers to the spatial distribution of the piezometric head, whereas the contour lines are in black.

We perform the same analysis for the decomposition-ED scenario and collect all the numerical results in Tables 3, 4, and 5. Again, the use of AR allows us to achieve an accuracy comparable to the UR test cases with less elements in both the matrix mesh (**#-matr.**), and the fracture mesh (**#-frac.**).

In Fig. 10 we observe that the piezometric head profile computed along line AA′ converges to the reference solution by increasing the number of refinements for all the numerical simulations. We point out that, while the embedded-ED test cases reveal large discrepancies with respect to the reference solution in the region of the left fracture, only little differences are observed for the decomposition-ED scenarios. Indeed, the mortar approach requires a matching geometry at

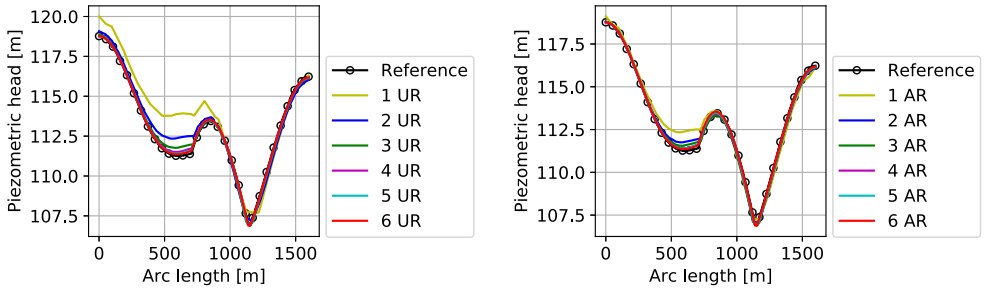

(a) Uniform Refinement (UR) (b) Adaptive Refinement (AR)

Fig. 9. *2D Benchmark Case 2: Hydrocoin.* Pressure along line AA′ for the uniform (A) and the adaptive (B) Embedded-ED test cases. Here, UR and AR refer to different steps of uniform and adaptive refinements performed on the initial matrix mesh. In particular, the number of AR are obtained combining a gradient recovery strategy with an adaptive refinement performed on the overlapping region between the matrix and the fracture zone. More details can be found in Tables 3, 4, and 5.

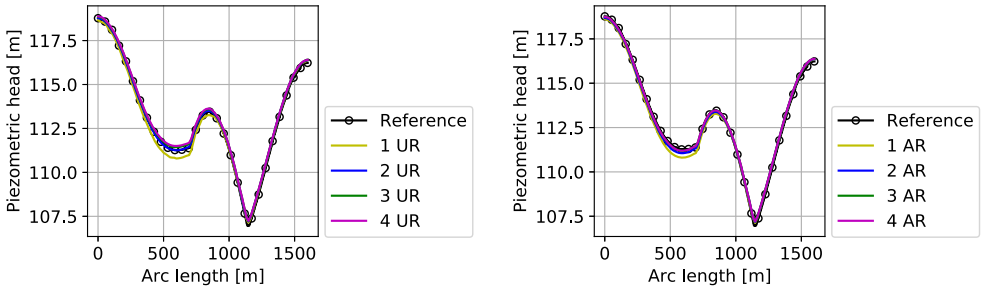

(a) Uniform Refinement (UR) (b) Adaptive Refinement (AR)

Fig. 10. *2D Benchmark Case 2: Hydrocoin.* Pressure along line AA′ for the uniform (A) and the adaptive (B) Decomposition-ED test cases. Again, UR and AR refer to the steps of uniform and adaptive refinement performed on the initial matrix mesh. We use a solution computed on a very fine mesh with 2745606 nodes as a reference.

the interface between fracture and matrix, and consequently more accurate results are achieved even with coarser meshes as confirmed also by the error analysis.

Even though the use of AR allows to compute accurate results also on coarse meshes, the non-conforming adaptive mesh strategy we adopted negatively affects the conditioning of the overall problem. Indeed, the condition numbers reported in Tables 3-5, reveal that UR test cases produce values which are several order of magnitudes lower than the ones computed on AR meshes. Ill-conditioning associated with anisotropic AR meshes is a well known problem which can be alleviated by adopting suitable preconditioning techniques. We address this problem, as suggested by Kamenski et al. [88], by means of diagonal scaling. This operation reduces the effects of mesh non-uniformity, and, in our experiments, consistently reduces the order of magnitude of the condition number in half (e.g., 10^{12} becomes approximately 10^{6}).

3.1.3. 2D benchmark case 3: realistic fracture network

We consider the same settings and reference solution used in Flemisch et al. [38] *Benchmark 4*. For this benchmark, a more realistic fracture network is taken into consideration. Here, the size of the domain is 700 m x 600 m with a fracture network of 64 fractures divided in 13 connected groups. The matrix permeability is $\mathbf{K} = \mathbf{I} \cdot 10^{-14}$ m^2. All the fractures have the same permeability 10^{-8} m^2 and the same aperture $\epsilon = 10^{-2}$ m. Hence, we have $\mathbf{K}_{\gamma^1} = \epsilon \mathbf{I} \cdot 10^{-8}$ for the HD case, and $\mathbf{K}_{\gamma^2} = \mathbf{I} \cdot 10^{-8}$ for the ED one. There are no-flow boundary conditions on top and bottom of the domain. A pressure of 1 013 250 Pa is imposed on the left boundary and of 0 Pa on the right boundary. Due to the rather complex geometry of the fracture network, the mortar decomposition method is impractical, hence it is not used here. We exclusively present results for the equi-dimensional embedded method. The mesh of the matrix has been automatically refined at the intersection with the fracture, for each experiment with 3, 6, and 7 levels of non-conforming mesh refinement, respectively. It can be observed in Table 6 the condition numbers have comparable magnitudes for both HD and ED versions. The condition number becomes large with the extremely varying mesh size resulting from the heavily focused refinement around the fractures. In fact, as can be observed in Table 6 (b), when the mesh is refined uniformly the condition number is typically several order of magnitudes lower.

Table 6
2D Benchmark Case 3: Realistic fracture network from Flemisch et al. [38]. Mesh information (number of elements and degrees of freedom), characteristics of system matrix and error in the matrix computed with respect to the reference solution for Emebedded equidimensional (ED) and hybriddimensional (HD) methods. Table (a) reports the results obtained by locally refining the mesh around fractures. Table (b) reports the results in case of uniform mesh refinement. Mesh information, characteristics of system matrix and error in the matrix for the *2D Realistic fracture network* benchmark in Embedded-ED and Embedded-HD cases.

Method	#-matr.	#-frac.	d.o.f.	nnz/size^2	$\|\cdot\|_2$-cond.
Embedded-ED	1405 quads	199 996	1487	1.9e-4	2.0e15
Embedded-ED	39 085 quads	199 996	41 773	2.3e-4	2.2e17
Embedded-ED	94 513 quads	199 996	102 486	9.1e-5	5.8e17
Embedded-HD	4200 quads	1024	4331	3.8e-3	1.3e16
Embedded-HD	67 200 quads	4096	67 721	1.6e-4	2.1e17

(a) Local mesh refinement around fractures

Method	#-matr.	#-frac.	d.o.f.	nnz/size^2	$\|\cdot\|_2$-cond.
Embedded-ED	1600 quads	199 996	1681	2.1e-3	4.2e5
Embedded-ED	25 600 quads	199 996	25 921	7.4e-5	2.0e7
Embedded-ED	102 400 quads	199 996	103 041	1.4e-5	1.7e8
Embedded-HD	6400 quads	2048	6561	4.8e-4	1.9e6
Embedded-HD	102 400 quads	2048	103 041	3.3e-5	1.6e8

(b) Uniform mesh refinement

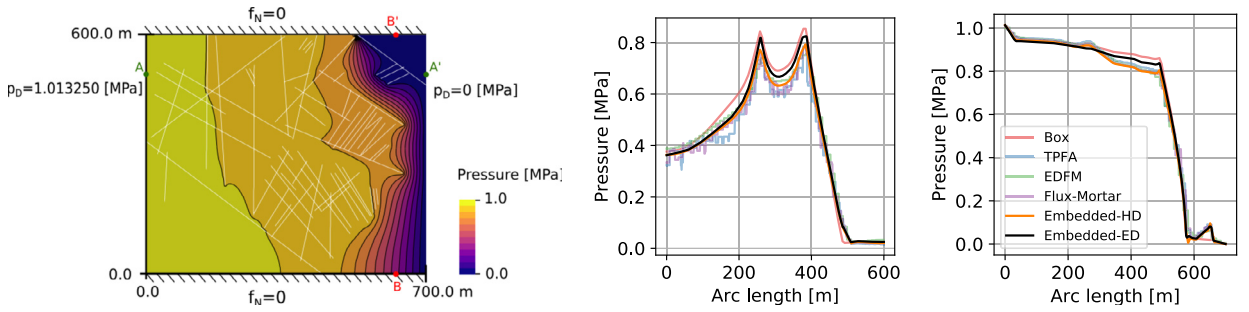

(a) Pressure solution (b) Line AA′ (c) Line BB′

Fig. 11. *2D Benchmark Case 3: Realistic fracture network*, from Flemisch et al. [38]. Pressure solution for real fracture network with 64 fractures (a). Pressure profiles along the lines (b) AA′nd (c) BB′ for both Embedded-HD and Embedded-ED techniques.

As can be observed in Fig. 11, the results obtained are similar to those obtained by other methods in the field although no reference solution is available. It can be noticed that the equi-dimensional variant is closer to the *Box* method compared to most other methods, including the hybrid dimensional results presented in [60]. From a practical perspective the equi-dimensional technique is slightly more complex since the fractures are extruded in normal direction, although automatically, thus requiring many more elements.

3.2. 3D experiments

Flow through fractured porous media is largely governed by 3D effects. Therefore, this section presents an application and evaluation of the dual Lagrange multiplier methods in 3D. First, results obtained with three Lagrange multiplier methods (embedded HD, embedded ED, decomposition HD) are compared to results of 17 methods presented in the benchmark study by Berre et al. [85]. More complex benchmark cases in 3D are studied for the embedded HD method as part of the aforementioned benchmark study. The embedded HD method is preferably used for those geometrically complex cases as it eases meshing of the fracture networks and the porous matrix mesh can be chosen regular. Fracture network mesh generation for the embedded ED method is more challenging, which is particularly relevant at the fracture intersection. Furthermore, all 3D benchmark cases in [85] are designed for very small fracture apertures and therefore equi-dimensional fracture meshes result in poor mesh quality. It is also important to bear in mind that equi-dimensional fracture meshes are mainly necessary for large aperture values and the benchmark cases yield no reason to use equi-dimensional meshes. Furthermore, the decomposition approach based on the mortar method is less suited for complex fracture geometries due to the complexity of both, setting up the mesh and dealing with over-constrained scenarios for the mortar conditions. In a final complex scenario the strength of each method is demonstrated and they are applied in a combined scenario as it could be typical for fractured systems. The experiments are in agreement with the expected results for studying flow problems.

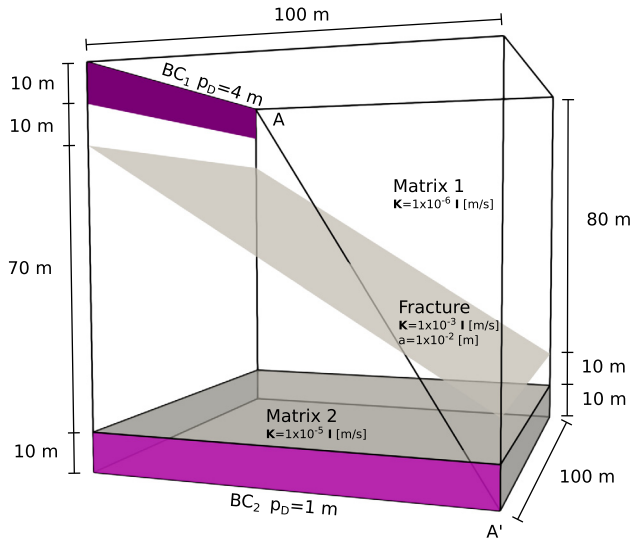

Fig. 12. *3D Benchmark Case 1: Single fracture.* Model domain (outlines) of benchmark *Case 1: Single Fracture* in Berre et al. [85] with Matrix 1 and 2 and a single fracture intersecting Matrix 1. Boundary 1 (BC_1) is the inflow and boundary 2 (BC_2) the outflow. Results are compared along the line AA′ through the matrix domains.

Note that, while in these studies there are no evident problems related to the lack of local mass conservation of the finite element discretization, further investigations are envisioned to improve on this aspect and for extending these studies to transport problems.

3.2.1. 3D benchmark case 1: single fracture

In this section three Lagrange multiplier methods are compared to benchmark *Case 1: Single Fracture* presented by Berre et al. [85], which is simple enough to accommodate all the fracture representations in one single study, including the different versions of the decomposition approach. This presentation also includes results obtained with the hybrid embedded method, presented in Schädle et al. [60]. Nevertheless, for completeness and for better comparison of the methods presented in this study the results of the hybrid embedded approach are again explicitly presented. To ease comparison, the results presented in the benchmark study are summarized and only the mean of all results as well as the standard deviation are plotted. The comparison of vastly different discretization methods is enabled by interpolating each solution to 1000 evenly spaced points along a line. Following this, the mean and standard deviation are computed at each of these points. It is important to note that the mean of all results is not necessarily the correct solution and just provides a measure of comparison to the results presented in the aforementioned benchmark study. For the detailed benchmark results the interested reader is referred to Berre et al. [85]. Finally, improvements of the accuracy can be demonstrated for the embedded ED approach by adaptive mesh refinement.

Fig. 12 shows the model domain of benchmark *Case 1: Single Fracture* which is adapted from Zielke et al. [89] and Barlag et al. [90]. This case consists of a single fracture intersecting a matrix cube with 100 m edge length. The lowest 10 m thick layer of the matrix block (Matrix 2) has an increased permeability. Fluid injection occurs at a Dirichlet boundary condition (BC_1) located above the fracture at the upper most 10 m thick layer of the matrix block. A Dirichlet boundary condition (BC_2) which acts as the outflow, is located at Matrix 2. The injection pressure is fixed at 4 m and the production pressure at 1 m. The permeability $\mathbf{K}$ in the Matrix 1 is $\mathbf{I} \cdot 10^{-6}$ [m/s] and in the Matrix 2 $\mathbf{I} \cdot 10^{-5}$ [m/s]. The fracture has a permeability $\mathbf{K}_\gamma$ of $\mathbf{I}_\gamma \cdot 10^{-3}$ [m/s] with an aperture ϵ of 10^{-2} [m].

The results obtained with the hybrid- and equi-dimensional embedded method and the hybrid decomposition method are presented in Fig. 13. In the upper part of the figure, three different mesh sizes (∼1k, ∼10k, and ∼100k matrix cells) are compared to 17 methods presented in Berre et al. [85]. It is important to keep in mind that the hybrid-dimensional embedded results are also part of the benchmark results. The pressure solution for all methods is compared along the line AA′ (see Fig. 12).

Overall, the results of the methods presented here and the methods presented in Berre et al. [85] show good convergence towards a common solution. Particularly for the very coarse mesh of only ∼1k cells in the matrix domains the Lagrange multiplier methods show some deviations. These deviations are more pronounced for the embedded HD method at the first half of line AA′ and for the embedded ED and the decomposition method at the second half. The deviations are partially due to the fact that most of the other methods presented in the benchmark study represent the fracture geometry in the matrix explicitly in matching mesh geometries. Embedded techniques typically require a resolution that is roughly twice as high as fitted mesh techniques to achieve the same accuracy. Already for the case with ∼10k cells the embedded HD and ED methods show very similar results. For the coarsest case neither of the methods is preferable as they all show deviations

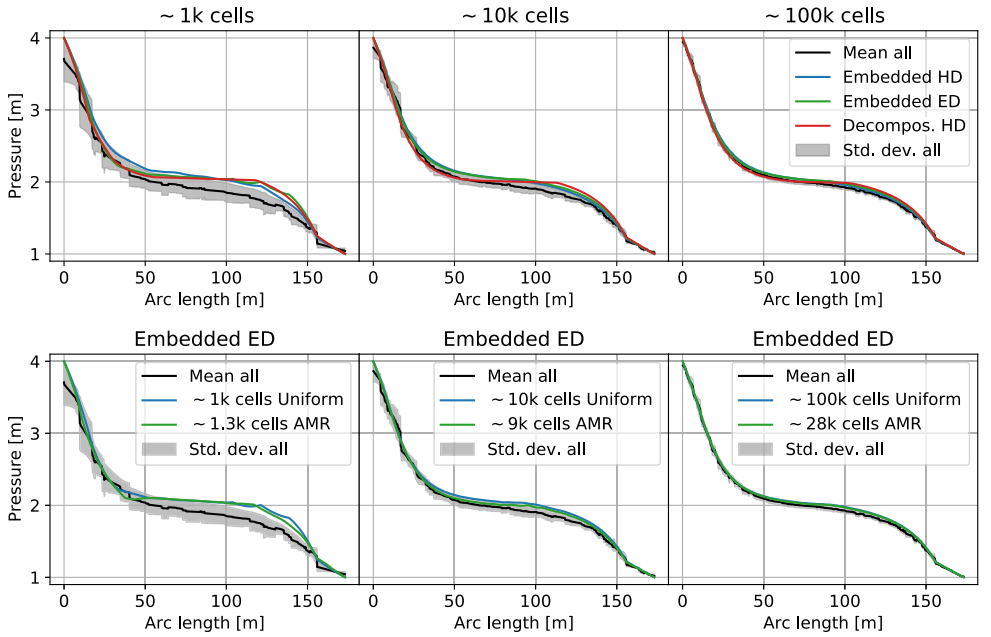

Fig. 13. *3D Benchmark Case 1: Single fracture.* Pressure results along the line AA′ for ∼1k, ∼10k, and ∼100k matrix cells for uniform refinement (upper figure) and ∼1.3k, ∼9k, and ∼28k for adaptive mesh refinement (lower figure). Results are shown with uniform refinement for the hybrid-dimensional (HD) and equi-dimensional (ED) embedded method and the hybrid decomposition method and with adaptive mesh refinement for the equi-dimensional embedded method. The black line shows the mean results of all benchmark methods and the grey range shows the standard deviation, respectively [85].

in different regions. Furthermore, the solution of the decomposition method shows a kink at ∼ 115 m for all mesh sizes. As mentioned above, this is due to over-constrained dofs, which poses significant technical challenges to be automated in 3D.

As shown in 3.1.2 adaptive mesh refinement allows to obtain more accurate results while reducing the number of matrix elements. Here the matrix mesh for the embedded ED approach is adaptively refined with up to two refinement steps, starting at ∼500 cells by progressively reducing the threshold of error adopted for the gradient recovery strategy. For brevity, we refer to the error threshold as $\mathbf{err}_g$ and to the number of adaptive refinement steps as AR. Thus, we employ $\mathbf{err}_g = 15$ and $\mathrm{AR} = 1$ for the coarsest mesh, $\mathbf{err}_g = 5$ and $\mathrm{AR} = 2$ for the middle mesh, and $\mathbf{err}_g = 0.1$ and $\mathrm{AR} = 2$ for the finest test case. One may note that the error threshold, $\mathbf{err}_g$, is progressively reduced to increase the accuracy of the numerical results. The matrix meshes resulting from the adaptive mesh refinement have ∼1.3k, ∼9k, and ∼28k cells. In Fig. 13, second row, we compare the results obtained with uniformly refined meshes with those obtained with adaptive mesh refinement. While the AMR has some more cells than the compared uniform mesh, the pressure solution along parts of the line AA′ is closer to the mean of all benchmark methods. For the two finer meshes, an improvement in accuracy is clearly visible. Taken together, all Lagrange multiplier methods presented here show good convergence and match well with other methods presented in the benchmark study.

3.3. Complex 3D scenario

Geological setting with fractures and faults often require to represent such features with permeability and aperture values ranging over several orders of magnitude. Therefore, their combined representation in numerical models is crucial for a complete description of geological settings. The setup of the present, more realistic, scenario is loosely based on the geological setting at the Grimsel Test Site, (GTS) [91]. However, it is important to note that the steady-state flow field, as computed here, is difficult to achieve in experiments conducted in such laboratories with a very low permeability rock matrix. Nevertheless, the given setup allows to demonstrate the different strength of the particular methods described in this study, i.e. complex fracture networks, fractures with large aperture widths, and blocking fractures. Even more importantly, the given scenario shows the integration of several coupling strategies in a single joint framework method.

Fig. 14 shows the model domain with a complex fracture network (blue) located between two large features with two intersecting fractures each. One of these features acts as blocking fractures (yellow) with low permeability values, the fractures in the other feature have large apertures (magenta). Furthermore, two boreholes are drilled into the rock domain with one of them ending in the large aperture fractures and the other one in the rock domain. The upper right corner of the square domain is not modeled as it acts as an access tunnel with atmospheric pressure. Consequently, the pressure at the outer boundary is fixed by a Dirichlet boundary condition of $p_D = (x - y + 100)\, 0.025$ (green). This boundary condition results in a pressure of 1 MPa at the access tunnel location and 5 MPa at the lower right corner. At the top and bottom (z-direction) of the domain no-flow boundary conditions are applied.

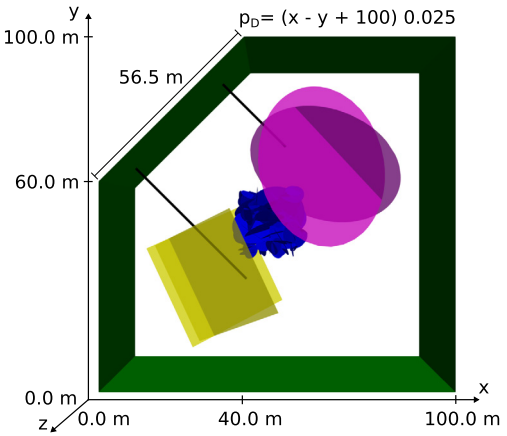

Fig. 14. *Complex 3D scenario.* Model domain of the complex case with a combined application of all presented methods. The upper right corner represents a ventilated access tunnel, as it is typical in deep underground laboratories. Fractures computed with the hybrid embedded method are depicted in blue and fractures computed with the equi-dimensional embedded method in pink. The yellow domains, with low permeability, are equi-dimensional and coupled by the mortar method. The green planes show the outer boundaries and the black lines indicate the injection and production boreholes.

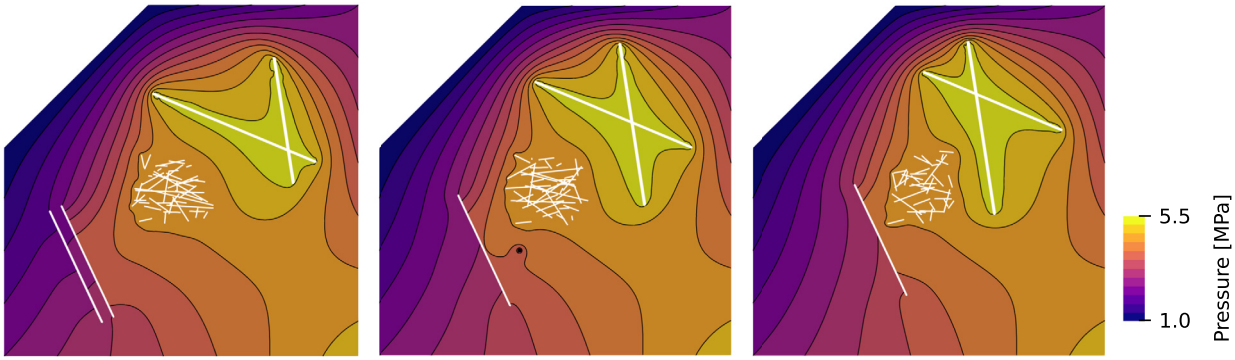

(a) Plane at $z = -5$ m (b) Plane at $z = 0$ m (c) Plane at $z = 5$ m

Fig. 15. *Complex 3D scenario.* Pressure solution at three planes intersecting the domain at -5 m, 0 m, and 5 m in z-direction.

In the numerical model the fractures and fracture network are represented by three different methods described above. The complex fracture network (blue) is meshed with lower-dimensional manifolds and embedded in the matrix mesh and has been initially presented by Schädle et al. [60]. In this study the fracture aperture and permeability and the matrix permeability are chosen so that the fractures and the matrix contribute similarly to the overall flow. In contrast, the rock matrix in the present experiment holds a low permeability and the fracture properties are chosen to dominate the flow. The fracture radius distribution in the network follows a power law, with truncations at 2.5 m and 10 m. The 150 fractures are circular, randomly oriented, and distributed in a cubical area of the model domain with a side length of 25 m. The fracture aperture is $\sim 10^{-4}$ m and the permeability chosen to be $\sim 10^{-9}$ m^2. Furthermore, the two fractures with large apertures (magenta) are represented by equi-dimensional domains embedded in the matrix domain. One of these fractures is intersected by a borehole which is explicitly meshed as a sub-domain. The two fractures are circular with an aperture width of 3×10^{-1} m and radii of 25 m. Further, the infilling material of these fractures is assumed to have a permeability of 1×10^{-12} m^2. In the borehole domain a forcing function of 1.0×10^{-13} is applied in a volume of 1×10^{-2} m^3, acting as an injection borehole with a pressure of ~5.5 MPa. To represent fractures with low permeability, acting as blocking fractures, two fractures (yellow) are described by equi-dimensional domains coupled to the matrix mesh by the mortar method (i.e., decomposition-ED). These fractures are rectangular with a side length of 35 m and permeability of 1×10^{-21} m^2. Generally, the fractures might be of any shape, e.g. circular or rectangular. The second borehole acts as a sink with a fixed pressure at 1 MPa. This borehole is represented by a separate small domain with the dimensions of the borehole itself and by using the decomposition-ED variant. Finally, the matrix permeability is 1×10^{-18} m^2.

Fig. 15 shows the pressure distribution across three planes intersecting the model domain parallel to the *xy*-plane. Throughout all planes the low permeability fractures act as discontinuities for pressure. Moreover, for plane (a) a clear discontinuity can be observed across the two fracture cross sections. With the high aperture and permeability of the complex fracture network and the low permeability of the rock matrix the pressure across the fracture network is equilibrated, connecting the upper right with the lower left part of the domain. With the injection borehole in one of the two equi-

dimensional fractures, these fractures and the surrounding rock matrix area are subject to the largest pressure values. In plane (b) the production borehole locally reduces the pressure to atmospheric pressure. However, due to the low permeability of the rock matrix the gradient around this borehole is very steep and the influence on the overall solution is limited. Additionally, the fixed pressure boundary condition at the outer boundary forces the pressure to steep gradients close to the embedded ED fractures with high injection pressure. These steep gradients result from boundary effects and for a representative study of such a geological setting the domain would have to be extended in these areas. However, the goal of this study is to demonstrate the application of Lagrange multipliers for different coupling strategies, spanning from equi-dimensional to lower dimensional models, and from embedded to mortar techniques. Ultimately, this allows more flexibility in the treatment of the fracture and the matrix configuration. Furthermore, such steep gradients are generally difficult to resolve in numerical models, thus adding further complexity to this test case. In summary, this complex 3D scenario demonstrates the strength of each method and the ability of the presented unified framework to combine all of these approaches while yielding smooth pressure results in geologically complex settings. More specifically, the hybrid-dimensional embedded approach eases meshing of complex fracture networks of fractures with small aperture widths, the equi-dimensional embedded approach allows to consider fractures with large aperture widths, and the equi-dimensional mortar approach enables to consider blocking fractures.

4. Conclusion

This study expands on previous works based on the application of the Lagrange multiplier method to compute single-phase fluid flow problems in fracture dominated porous media. In particular, we employ the finite element method in combination with an L^2-projection operator to couple different types of non-conforming meshes. The non-conformity might arise at the interface of independently meshed sub-domains, at hanging nodes resulting from adaptive mesh refinement, or by combining multiple overlapping meshes. Furthermore, fractures are either described by equi-dimensional or hybrid-dimensional domains. The applied Lagrange multiplier is discretized using dual basis functions, which provide two main advantages. First, the number of degrees of freedom is reduced to the ones of the background mesh representing the porous-matrix. Second, the arising symmetric-positive-definite linear systems are convenient to work with.

Here, we present a unified framework covering all coupling techniques mentioned above. The different mesh solutions are compared to state-of-the-art benchmark cases in 2D and 3D, the numerical performance is studied, and use cases are presented in isolation and combination. Overall, the results suggest that the presented tool-set is capable of computing fluid-flow through complex and heterogeneous rock formations in a robust and convenient way. It is important to bear in mind that realistic scenarios of fracture dominated rock formations may include fractures with geometric and physical properties ranging over many orders of magnitude. Therefore, the presented single joint framework allows to deeply exploit non-conforming hybrid- and equi-dimensional fracture models and efficiently combine these models. By using the dual Lagrange multiplier we are able to combine multiple complex fracture networks without changing the size of the algebraic system arising from the porous-medium matrix, although we have more non-zero entries associated with the coupled degrees of freedom. It is also worth to point out that the conditioning of the system is not worsened, as it is the case when using other types of Lagrange multipliers [60].

With the integration of adaptive mesh refinement in the solution process, the error in the solution can be controlled in an automated way either by means of an error estimator or by pre-defining areas of interest for refinement. This allowed to complement the discussion in Schädle et al. [60] about the necessity of having a finer mesh around fractures and their tips and intersections.

The study of a complex, more realistic, geological setting, inspired by the Grimsel Test Site, demonstrates the advantage of the unified framework to represent vastly different fracture geometries and properties within a single numerical model. This allows to expand on existing numerical studies of such systems by the opportunity to include a large range of fracture representations. Furthermore, the highly efficient and convenient tools combined with the eased meshing of non-conforming meshes enable stochastic studies for a wide range of fracture dominated systems.

Further investigations based on this unified framework would benefit by focusing on mass conservation properties of the finite element discretization and application to transport problems.

CRediT authorship contribution statement

Patrick Zulian: Conceptualization, Investigation, Methodology, Software, Visualization, Writing – original draft, Writing – review & editing. **Philipp Schädle:** Data curation, Investigation, Visualization, Writing – original draft. **Liudmila Karagyaur:** Data curation, Investigation, Visualization, Writing – original draft, Writing – review & editing. **Maria G.C. Nestola:** Data curation, Investigation, Software, Visualization, Writing – original draft, Writing – review & editing.

Declaration of competing interest

The authors declare that they have no known competing financial interests or personal relationships that could have appeared to influence the work reported in this paper.

Computer code availability

All methods and routines, used for this study, are implemented with the open-source software library *Utopia* [80,81]. *Utopia*'s lead developer is author Patrick Zulian at USI Lugano, Switzerland. The contact address and e-mail of Patrick Zulian are as follows:

Euler institute
Università della Svizzera italiana (USI - University of Lugano)
Via Giuseppe Buffi 13
CH-6900 Lugano

patrick.zulian@usi.ch

Utopia was first available in 2016, the programming language is *C++* and it can be accessed through a git repository or a docker container on:

https://bitbucket.org/zulianp/utopia (approx. 40 MB of uncompressed data),
https://hub.docker.com/r/utopiadev/utopia.

The software dependencies are as follows:

PETSc (https://www.mcs.anl.gov/petsc),
must be compiled with *HYPRE* enabled
libMesh for the FE module (https://github.com/libMesh)

There are no hardware requirements given by *Utopia*. Potential hardware or software requirements of the underlying libraries *libMesh* and *PETSc* are not stated here.

Acknowledgement

P.Z., M.G.C.N., and L.K. thank the SCCER-SoE and SCCER-FURIES programs. This work was supported by a grant from the Swiss National Supercomputing Centre (CSCS) under the project FASTER: Forecasting and Assessing Seismicity and Thermal Evolution in geothermal Reservoirs. P.S. thanks the Werner Siemens Foundation for their endowment of the Geothermal Energy and Geofluids group at the Institute of Geophysics, ETH Zurich.

The authors thank the anonymous reviewers for the valuable feedback which helped improving the content and presentation of this paper.

References

[1] A. Pochon, J.-P. Tripet, R. Kozel, B. Meylan, M. Sinreich, F. Zwahlen, Groundwater protection in fractured media: a vulnerability-based approach for delineating protection zones in Switzerland, Hydrogeol. J. 16 (2008).
[2] T. Read, O. Bour, V. Bense, T. Le Borgne, P. Goderniaux, M. Klepikova, R. Hochreutener, N. Lavenant, V. Boschero, Characterizing groundwater flow and heat transport in fractured rock using fiber-optic distributed temperature sensing, Geophys. Res. Lett. 40 (2013) 2055–2059.
[3] J.W. Tester, B. Anderson, A. Batchelor, D. Blackwell, R. DiPippo, E. Drake, J. Garnish, B. Livesay, M.C. Moore, K. Nichols, et al., The Future of Geothermal Energy: Impact of Enhanced Geothermal Systems (EGS) on the United States in the 21st Century, vol. 209, Massachusetts Institute of Technology, 2006.
[4] M.W. McClure, R.N. Horne, Correlations between formation properties and induced seismicity during high pressure injection into granitic rock, Eng. Geol. 175 (2014) 74–80.
[5] C.E. Bond, R. Wightman, P.S. Ringrose, The influence of fracture anisotropy on co2 flow, Geophys. Res. Lett. 40 (2003) 1284–1289.
[6] E. Bonnet, O. Bour, N.E. Odling, P. Davy, I. Main, P. Cowie, B. Berkowitz, Scaling of fracture systems in geological media, Rev. Geophys. 39 (2001) 347–383.
[7] A. Rasmuson, I. Neretnieks, Radionuclide transport in fast channels in crystalline rock, Water Resour. Res. 22 (1986) 1247–1256.
[8] F. Amann, V. Gischig, K. Evans, J. Doetsch, R. Jalali, B. Valley, H. Krietsch, N. Dutler, L. Villiger, B. Brixel, et al., The seismo-hydromechanical behavior during deep geothermal reservoir stimulations: open questions tackled in a decameter-scale in situ stimulation experiment, Solid Earth 9 (2018) 115–137.
[9] J.-R. de Dreuzy, Y. Méheust, G. Pichot, Influence of fracture scale heterogeneity on the flow properties of three-dimensional discrete fracture networks (dfn), J. Geophys. Res., Solid Earth 117 (2012).
[10] R. Zimmerman, S. Kumar, G. Bodvarsson, Lubrication theory analysis of the permeability of rough-walled fractures, Int. J. Rock Mech. Min. Sci. Geomech. Abstr. 28 (1991) 325–331.
[11] A. Ebigbo, P.S. Lang, A. Paluszny, R.W. Zimmerman, Inclusion-based effective medium models for the permeability of a 3d fractured rock mass, Transp. Porous Media 113 (2016) 137–158.
[12] D. Vogler, F. Amann, P. Bayer, D. Elsworth, Permeability evolution in natural fractures subject to cyclic loading and gouge formation, Rock Mech. Rock Eng. 49 (2016) 3463–3479.
[13] S.P. Neuman, Stochastic approach to subsurface flow and transport: a view to the future, in: International Hydrology Series, Cambridge University Press, 1997, pp. 231–241.
[14] B. Berkowitz, Characterizing flow and transport in fractured geological media: a review, Adv. Water Resour. 25 (2002) 861–884.
[15] M.C. Cacas, E. Ledoux, G. Marsily, B. Tillie, A. Barbreau, E. Durand, B. Feuga, P. Peaudecerf, Modeling fracture flow with a stochastic discrete fracture network: calibration and validation: 1. The flow model, Water Resour. Res. 26 (1990) 479–489.

[16] A. Hobé, D. Vogler, M.P. Seybold, A. Ebigbo, R.R. Settgast, M.O. Saar, Estimating fluid flow rates through fracture networks using combinatorial optimization, Adv. Water Resour. 122 (2018) 85–97.
[17] S.P. Neuman, Trends, prospects and challenges in quantifying flow and transport through fractured rocks, Hydrogeol. J. 13 (2005) 124–147.
[18] J.-R. de Dreuzy, G. Pichot, B. Poirriez, J. Erhel, Synthetic benchmark for modeling flow in 3d fractured media, Comput. Geosci. 50 (2013) 59–71.
[19] B. Dessirier, C.-F. Tsang, A. Niemi, A new scripting library for modeling flow and transport in fractured rock with channel networks, Comput. Geosci. 111 (2018) 181–189.
[20] J. Warren, P. Root, The behavior of naturally fractured reservoirs, Soc. Pet. Eng. J. 3 (1963) 245–255.
[21] G. Barenblatt, I.P. Zheltov, I. Kochina, Basic concepts in the theory of seepage of homogeneous liquids in fissured rocks [strata], J. Appl. Math. Mech. 24 (1960) 1286–1303.
[22] H. Kazemi, Pressure transient analysis of naturally fractured reservoirs with uniform fracture distribution, Soc. Pet. Eng. J. 9 (1969) 451–462.
[23] H. Kazemi, L. Merrill Jr, K. Porterfield, P. Zeman, et al., Numerical simulation of water-oil flow in naturally fractured reservoirs, Soc. Pet. Eng. J. 16 (1976) 317–326.
[24] J. Noorishad, M. Mehran, An upstream finite element method for solution of transient transport equation in fractured porous media, Water Resour. Res. 18 (1982) 588–596.
[25] R.G. Baca, R.C. Arnett, D.W. Langford, Modelling fluid flow in fractured-porous rock masses by finite-element techniques, Int. J. Numer. Methods Fluids 4 (1984) 337–348.
[26] J.D. Hyman, S. Karra, N. Makedonska, C.W. Gable, S.L. Painter, H.S. Viswanathan, dfnworks: a discrete fracture network framework for modeling subsurface flow and transport, Comput. Geosci. 84 (2015) 10–19.
[27] B. Flemisch, M. Darcis, K. Erbertseder, B. Faigle, A. Lauser, K. Mosthaf, S. Müthing, P. Nuske, A. Tatomir, M. Wolff, H. Rainer, Dumux: dune for multi-{phase, component, scale, physics,…} flow and transport in porous media, Adv. Water Resour. 34 (2011) 1102–1112.
[28] K. Lipnikov, G. Manzini, M. Shashkov, Mimetic finite difference method, J. Comput. Phys. 257 (2014) 1163–1227.
[29] I.-H. Lee, C.-F. Ni, Fracture-based modeling of complex flow and co2 migration in three-dimensional fractured rocks, Comput. Geosci. 81 (2015) 64–77.
[30] I.-H. Lee, C.-F. Ni, F.-P. Lin, C.-P. Lin, C.-C. Ke, Stochastic modeling of flow and conservative transport in three-dimensional discrete fracture networks, Hydrol. Earth Syst. Sci. 23 (2019) 19–34.
[31] M. Cacace, G. Blöcher, Meshit—a software for three dimensional volumetric meshing of complex faulted reservoirs, Environ. Earth Sci. 74 (2015) 5191–5209.
[32] R. Holm, R. Kaufmann, B.-O. Heimsund, E. Øian, M.S. Espedal, Meshing of domains with complex internal geometries, Numer. Linear Algebra Appl. 13 (2006) 717–731.
[33] D. Blessent, R. Therrien, K. MacQuarrie, Coupling geological and numerical models to simulate groundwater flow and contaminant transport in fractured media, Comput. Geosci. 35 (2009) 1897–1906.
[34] M. Karimi-Fard, L. Durlofsky, K. Aziz, An efficient discrete-fracture model applicable for general-purpose reservoir simulators, SPE J. 9 (2004) 227–236.
[35] I. Bogdanov, V. Mourzenko, J.-F. Thovert, P. Adler, Two-phase flow through fractured porous media, Phys. Rev. E 68 (2003) 026703.
[36] J. Monteagudo, A. Firoozabadi, Control-volume method for numerical simulation of two-phase immiscible flow in two- and three-dimensional discrete-fractured media, Water Resour. Res. 40 (2004).
[37] R. Helmig, et al., Multiphase Flow and Transport Processes in the Subsurface: A Contribution to the Modeling of Hydrosystems, Springer-Verlag, 1997.
[38] B. Flemisch, I. Berre, W. Boon, A. Fumagalli, N. Schwenck, A. Scotti, I. Stefansson, A. Tatomir, Benchmarks for single-phase flow in fractured porous media, Adv. Water Resour. 111 (2018) 239–258.
[39] E. Keilegavlen, R. Berge, A. Fumagalli, M. Starnoni, I. Stefansson, J. Varela, I. Berre, Porepy: an open-source software for simulation of multiphysics processes in fractured porous media, Comput. Geosci. (2020) 1–23.
[40] J.M. Nordbotten, W.M. Boon, A. Fumagalli, E. Keilegavlen, Unified approach to discretization of flow in fractured porous media, Comput. Geosci. 23 (2019) 225–237.
[41] P. Devloo, W. Teng, C.-S. Zhang, Multiscale hybrid-mixed finite element method for flow simulation in fractured porous media, Comput. Model. Eng. Sci. 119 (2019) 145–163.
[42] O. Duran, P.R.B. Devloo, S.M. Gomes, F. Valentin, A multiscale hybrid method for Darcy's problems using mixed finite element local solvers, Comput. Methods Appl. Mech. Eng. 354 (2019) 213–244.
[43] K. Brenner, M. Groza, C. Guichard, G. Lebeau, R. Masson, Gradient discretization of hybrid dimensional Darcy flows in fractured porous media, Numer. Math. 134 (2016) 569–609.
[44] K. Brenner, J. Hennicker, R. Masson, P. Samier, Gradient discretization of hybrid-dimensional Darcy flow in fractured porous media with discontinuous pressures at matrix–fracture interfaces, IMA J. Numer. Anal. 37 (2016) 1551–1585.
[45] C. Facciolà, P.F. Antonietti, M. Verani, Mixed-primal discontinuous Galerkin approximation of flows in fractured porous media on polygonal and polyhedral grids, PAMM 19 (2019) e201900117.
[46] L. Li, S.H. Lee, Efficient field-scale simulation of black oil in a naturally fractured reservoir through discrete fracture networks and homogenized media, SPE Reserv. Eval. Eng. 11 (2008) 750–758.
[47] H. Hajibeygi, D.C. Karvounis, P. Jenny, A hierarchical fracture model for the iterative multiscale finite volume method, J. Comput. Phys. 230 (2011) 8729–8743.
[48] M. Ţene, S.B. Bosma, M.S. Al Kobaisi, H. Hajibeygi, Projection-based embedded discrete fracture model (pedfm), Adv. Water Resour. 105 (2017) 205–216.
[49] A. Moinfar, A. Varavei, K. Sepehrnoori, R.T. Johns, Development of an efficient embedded discrete fracture model for 3D compositional reservoir simulation in fractured reservoirs, SPE J. 19 (2014) 289–303.
[50] K.D. Nikitin, R.M. Yanbarisov, Monotone embedded discrete fractures method for flows in porous media, J. Comput. Appl. Math. 364 (2020) 112353.
[51] B. Flemisch, A. Fumagalli, A. Scotti, A review of the XFEM-based approximation of flow in fractured porous media, in: Advances in Discretization Methods, Springer International Publishing, 2016, pp. 47–76.
[52] Z. Xu, Y. Yang, The hybrid dimensional representation of permeability tensor: a reinterpretation of the discrete fracture model and its extension on nonconforming meshes, J. Comput. Phys. 415 (2020) 109523.
[53] D. Capatina, R. Luce, H. El-Otmany, N. Barrau, Nitsche's extended finite element method for a fracture model in porous media, Appl. Anal. 95 (2016) 2224–2242.
[54] H. Huang, T.A. Long, J. Wan, W.P. Brown, On the use of enriched finite element method to model subsurface features in porous media flow problems, Comput. Geosci. 15 (2011) 721–736.
[55] N. Schwenck, B. Flemisch, R. Helmig, B.I. Wohlmuth, Dimensionally reduced flow models in fractured porous media: crossings and boundaries, Comput. Geosci. 19 (2015) 1219–1230.
[56] C. D'Angelo, A. Scotti, A mixed finite element method for Darcy flow in fractured porous media with non-matching grids, ESAIM: Math. Model. Numer. Anal. 46 (2012) 465–489.
[57] A. Fumagalli, A. Scotti, A numerical method for two-phase flow in fractured porous media with non-matching grids, Adv. Water Resour. 62 (2013) 454–464.
[58] A. Fumagalli, E. Keilegavlen, S. Scialò, Conforming, non-conforming and non-matching discretization couplings in discrete fracture network simulations, J. Comput. Phys. 376 (2019) 694–712.

[59] M. Köppel, V. Martin, J. Jaffré, J.E. Roberts, A Lagrange multiplier method for a discrete fracture model for flow in porous media, Comput. Geosci. 23 (2018) 239–253.
[60] P. Schädle, P. Zulian, D. Vogler, S.R. Bhopalam, M.G. Nestola, A. Ebigbo, R. Krause, M.O. Saar, 3d non-conforming mesh model for flow in fractured porous media using Lagrange multipliers, Comput. Geosci. 132 (2019) 42–55.
[61] I. Berre, F. Doster, E. Keilegavlen, Flow in fractured porous media: a review of conceptual models and discretization approaches, Transp. Porous Media 130 (2019) 215–236.
[62] M.G.C. Nestola, B. Becsek, H. Zolfaghari, P. Zulian, D.D. Marinis, R. Krause, D. Obrist, An immersed boundary method for fluid-structure interaction based on variational transfer, J. Comput. Phys. 398 (2019) 108884.
[63] S. Osborn, P. Zulian, T. Benson, U. Villa, R. Krause, P.S. Vassilevski, Scalable hierarchical pde sampler for generating spatially correlated random fields using nonmatching meshes, Numer. Linear Algebra Appl. 25 (2018) e2146.
[64] R. Glowinski, T.-W. Pan, J. Periaux, A fictitious domain method for Dirichlet problem and applications, Comput. Methods Appl. Mech. Eng. 111 (1994) 283–303.
[65] C. Bernardi, Y. Maday, A.T. Patera, Domain decomposition by the mortar element method, in: Asymptotic and Numerical Methods for Partial Differential Equations with Critical Parameters, Springer, 1993, pp. 269–286.
[66] A. Popp, B.I. Wohlmuth, M.W. Gee, W.A. Wall, Dual quadratic mortar finite element methods for 3d finite deformation contact, SIAM J. Sci. Comput. 34 (2012) B421–B446.
[67] C. Von Planta, D. Vogler, X. Chen, M.G. Nestola, M.O. Saar, R. Krause, Simulation of hydro-mechanically coupled processes in rough rock fractures using an immersed boundary method and variational transfer operators, Comput. Geosci. 23 (2019) 1125–1140.
[68] N. Frih, V. Martin, J.E. Roberts, A. Saâda, Modeling fractures as interfaces with nonmatching grids, Comput. Geosci. 16 (2012) 1043–1060.
[69] W.M. Boon, J.M. Nordbotten, I. Yotov, Robust discretization of flow in fractured porous media, SIAM J. Numer. Anal. 56 (2018) 2203–2233.
[70] C. Hesch, A. Gil, A.A. Carreño, J. Bonet, P. Betsch, A mortar approach for fluid–structure interaction problems: immersed strategies for deformable and rigid bodies, Comput. Methods Appl. Mech. Eng. 278 (2014) 853–882.
[71] B.I. Wohlmuth, A mortar finite element method using dual spaces for the Lagrange multiplier, SIAM J. Numer. Anal. 38 (2000) 989–1012.
[72] W.L. Briggs, S.F. McCormick, A Multigrid Tutorial, vol. 72, Siam, 2000.
[73] Sobolev Spaces, Springer, Berlin Heidelberg, Berlin, Heidelberg, 2008, pp. 159–194.
[74] B.P. Lamichhane, R.P. Stevenson, B.I. Wohlmuth, Higher order mortar finite element methods in 3d with dual Lagrange multiplier bases, Numer. Math. 102 (2005) 93–121.
[75] M. Paz, W. Leigh, Static condensation and substructuring, in: Integrated Matrix Analysis of Structures, Springer, 2001, pp. 239–260.
[76] D. Krause, T. Dickopf, M. Potse, R. Krause, Towards a large-scale scalable adaptive heart model using shallow tree meshes, J. Comput. Phys. 298 (2015) 79–94.
[77] P. Farah, W.A. Wall, A. Popp, A mortar finite element approach for point, line, and surface contact, Int. J. Numer. Methods Eng. 114 (2018) 255–291.
[78] I.E. Sutherland, G.W. Hodgman, Reentrant polygon clipping, Commun. ACM 17 (1974) 32–42.
[79] J. Cerveny, V. Dobrev, T. Kolev, Nonconforming Mesh Refinement for High-Order Finite Elements, 2019.
[80] P. Zulian, A. Kopaničáková, M.C.G. Nestola, A. Fink, N. Fadel, V. Magri, T. Schneider, E. Botter, Utopia: a C++ embedded domain specific language for scientific computing. Git repository, https://bitbucket.org/zulianp/utopia, 2016.
[81] P. Zulian, A. Kopaničáková, M.G.C. Nestola, N. Fadel, A. Fink, J. VandeVondele, R. Krause, Large scale simulation of pressure induced phase-field fracture propagation using Utopia, CCF Trans. High Perform. Comput. (2021).
[82] B.S. Kirk, J.W. Peterson, R.H. Stogner, G.F. Carey, libMesh: a C++ library for parallel adaptive mesh refinement/coarsening simulations, Eng. Comput. 22 (2006) 237–254.
[83] P. Zulian, ParMOONoLith: parallel intersection detection and automatic load-balancing library. Git repository, https://bitbucket.org/zulianp/par_moonolith, 2016.
[84] S. Balay, W.D. Gropp, L.C. McInnes, B.F. Smith, Efficient management of parallelism in object oriented numerical software libraries, in: E. Arge, A.M. Bruaset, H.P. Langtangen (Eds.), Modern Software Tools in Scientific Computing, Birkhäuser Press, 1997, pp. 163–202.
[85] I. Berre, W.M. Boon, B. Flemisch, A. Fumagalli, D. Gläser, E. Keilegavlen, A. Scotti, I. Stefansson, A. Tatomir, K. Brenner, S. Burbulla, P. Devloo, O. Duran, M. Favino, J. Hennicker, I.-H. Lee, K. Lipnikov, R. Masson, K. Mosthaf, M.G.C. Nestola, C.-F. Ni, K. Nikitin, P. Schädle, D. Svyatskiy, R. Yanbarisov, P. Zulian, Verification benchmarks for single-phase flow in three-dimensional fractured porous media, Adv. Water Resour. 147 (2021) 103759.
[86] N. Yan, A. Zhou, Gradient recovery type a posteriori error estimates for finite element approximations on irregular meshes, Comput. Methods Appl. Mech. Eng. 190 (2001) 4289–4299.
[87] T.J. Nicholson, T. McCartin, P.A. Davis, W. Beyeler, Nrc experiences in hydrocoin: an international project for studying ground-water flow modeling strategies, in: Waste Management'87: Waste Isolation in the US, Technical Programs, and Public Education, 1987.
[88] L. Kamenski, W. Huang, H. Xu, Conditioning of finite element equations with arbitrary anisotropic meshes, Math. Comput. 83 (2014) 2187–2211.
[89] W. Zielke, R. Helmig, K.P. Krohn, H. Shao, J. Wollrath, Discrete modelling of transport processes in fractured porous rock, in: 7th ISRM Congress, International Society for Rock Mechanics and Rock Engineering, 1991.
[90] C. Barlag, R. Hinkelmann, R. Helmig, W. Zielke, Adaptive methods for modelling transport processes in fractured subsurface systems, in: 3rd International Conference on Hydroscience and Engineering, Cottbus, vol. 284, Center of Computational Hydroscience and Engineering, The University of Mississippi, 1998.
[91] F. Amann, V. Gischig, K. Evans, J. Doetsch, R. Jalali, B. Valley, H. Krietsch, N. Dutler, L. Villiger, B. Brixel, M. Klepikova, A. Kittilä, C. Madonna, S. Wiemer, M.O. Saar, S. Loew, T. Driesner, H. Maurer, D. Giardini, The seismo-hydromechanical behavior during deep geothermal reservoir stimulations: open questions tackled in a decameter-scale in situ stimulation experiment, Solid Earth 9 (2018) 115–137.